



DEPTH SECTION IMAGING FOR PORTIONS OF AN
AIRBORNE GEOPHYSICAL SURVEY OF THE
HUNTON ANTICLINE, SOUTH-CENTRAL
OKLAHOMA

FINAL ADMINISTRATIVE REPORT
TO THE OKLAHOMA WATER RESOURCES BOARD
IN FULFILLMENT OF THE COOPERATIVE
AGREEMENT #08C7OK002032407

By

David V. Smith
Maryla Deszcz-Pan
Bruce D. Smith
U.S. Geological Survey
Denver, CO 80225

April 2009

CONTENTS

1.0 INTRODUCTION

2.0 EM1DFM INVERSION

2.1 Inversion Parameters

3.0 DEPTH OF INVESTIGATION

4.0 PRESENTATION

4.1 MultiPlots

4.2 Description of the MultiPlots

5.0 STRUCTURAL INTERPRETATION

5.1 Faults and Geologic Contacts

5.2 Epikarst and Soil

6.0 CONCLUSIONS

7.0 REFERENCES

Appendix 1. Block B MultiPlots

Appendix 2. Block D MultiPlots

1.0 INTRODUCTION

An airborne electromagnetic/magnetic survey was flown on behalf of the U.S. Geological Survey (USGS) by Fugro Airborne Surveys (Fugro) from March 13 to March 18, 2007, over four areas of interest located in the Arbuckle-Simpson aquifer area of the Hunton anticline in south-central Oklahoma (fig. 1). Survey coverage consisted of approximately 770.3 line-km, including 79.2 line-km of tie lines. The application of airborne electromagnetic surveys for ground-water mapping in karst environments has been described by Smith, Smith, and Blome (2008)

The objective of this survey (as is the case for all airborne electromagnetic methods) is to provide a detailed, densely sampled distribution of electrical resistivity with depth from ground surface to depths of 100-150 m. The correlation of resistivity with lithostratigraphic units improves our understanding of subsurface geology in a more efficient way than would be possible with drillholes or ground-based surveys.

To obtain information from varying depths it is necessary to use sensors that transmit electromagnetic waves at different frequencies because varying frequencies are attenuated differently in the earth: lower frequencies are attenuated less and provide

information from deeper parts; higher frequencies are attenuated more and penetrate to lesser depths. The term “apparent resistivity” refers to how the response of a constant earth (half-space) model of a uniform resistivity matches the observed data. When the measured signal at a given frequency is transformed to apparent resistivity and apparent depth (Fraser, 1978), these apparent values represent an average of all units above (and some below) the depth of penetration for this frequency. Apparent resistivity maps are very useful to show the lateral variations in resistivity at relative, albeit not constant, depths (shallower at higher frequencies, deeper at lower frequencies). However, these maps do not provide actual resistivity or depth values except in the very limited case when the geology is a homogeneous, uniform half-space.

A better approximation to the true distribution of resistivity with depth is accomplished using so-called differential resistivity and differential depth parameters (Huang and Fraser, 1996). This is a simple, stable method based on the transformation of measured data that does not require computationally intensive calculations required for the inversion of data. The differential parameters for the Arbuckle survey, provided by Fugro, consist of a resistivity and depth for each measured frequency. These resistivities and depths can be used to construct resistivity-depth inversion (RDI) sections.

Data were acquired using Fugro’s RESOLVE system (Fugro, 2009). Inversions of the RESOLVE data to produce resistivity-depth sections along each flight line were performed by closely following procedures developed by Condor Consulting, Inc. for an earlier helicopter electromagnetic (HEM) study of the Edwards aquifer at the north Seco Creek area in south-central Texas (Smith and others, 2003). The inversions were carried out using EM1DFM software developed by the University of British Columbia (Farquharson and Oldenburg, 2000).

2.0 EM1DFM INVERSIONS

The program EM1DFM (Farquharson and Oldenburg, 2004) was used to do one-dimensional (1-D) layered earth inversions on the HEM flight line data. This type of inversion is usually termed imaging since the number of layers is more than the number of frequencies at which measurements are made. This program inverts for resistivities of a user-specified number of layers with fixed, user-specified thicknesses that are constant throughout the survey. Application of this type of resistivity imaging in karst terrains was developed to interpret an HEM survey of the Edwards aquifer in the north Seco Creek area in south-central Texas (Smith and others, 2003). The layer thickness used for the HEM inversion of the Hunton anticline data are:

Upper depth (m)	Lower Depth (m)	Thickness (m)
0	-1.01	1.01
-1.01	-2.15	1.14
-2.15	-3.44	1.30
-3.44	-4.91	1.47
-4.91	-6.58	1.67
-6.58	-8.47	1.89

-8.47	-10.61	2.14
-10.61	-13.04	2.43
-13.04	-15.79	2.75
-15.79	-18.92	3.12
-18.92	-22.46	3.54
-22.46	-26.47	4.02
-26.47	-31.03	4.56
-31.03	-36.19	5.17
-36.19	-42.05	5.86
-42.05	-48.7	6.64
-48.7	-56.23	7.53
-56.23	-64.77	8.54
-64.77	-74.46	9.69
-74.46	-85.45	10.99
-85.45	-97.91	12.46
-97.91	-112.04	14.13
-112.04	-128.06	16.02
-128.06	-146.23	18.17
-146.23	-166.84	20.61
-166.84	-190.21	23.37
-190.21	-216.71	26.50

Underlying the deepest layer is a uniform half-space.

The 1-D inversion assumes that the layers are horizontal and of infinite extent. This approximation holds quite well providing dips of the strata are relatively low (less than approximately 30 degrees) and lateral changes in resistivity are relatively gradual. The inversions were carried out at every fiducial (approximately 3-m spacing along the flight lines).

The output of the inversions are presented as RDI sections, where the X- and Y-axes are in UTM, and the Z-axis is elevation above sea level (in meters). The resistivity values in each layer are shown as colors from blue (low resistivity) to red (high resistivity).

2.1 Inversion Parameters

Documentation for the EM1DFM program can be found at the University of British Columbia Inversion Facility website <http://www.eos.ubc.ca/ubcgif/> (valid as of February 23, 2009). Only data from the five coplanar frequencies (namely, 380, 1760, 6520, 26640, and 116400 Hz) were used in the inversion. Experimentation was carried out to establish the appropriate errors to apply to the data during inversion. The final choice of errors was 10 percent relative and 10 ppm absolute for all the channels, with the higher of these applied in each case.

Other EM1DFM inversion parameters (see EM1DFM documentation at <http://www.eos.ubc.ca/ubcgif/> for parameter description) were:

- Model Type — Conductivity only

- Start Model — 0.004 and 0.001 S/m (see below)
- Reference Model — 0.004 and 0.001 S/m (see below)
- Background Susceptibility Model — 0.0
- Inversion Type — Fixed Trade Off with B=10
- Maximum iterations — 25
- Tolerance — 0.001
- Reference Model closeness coefficient: *acs* — 0.001
- Reference Model flatness coefficient: *acz* — 1.0

3.0 DEPTH OF INVESTIGATION

As the depth increases, there is less signal to constrain the inversion because the response diminishes by approximately the cube of the distance from the conductive layer to the HEM bird (approximately 30 m above ground), and the computed conductivities trend more to the reference model. The reference model used was a constant conductivity for all layers (that is, a uniform half-space). The general approach was used in evaluation of the HEM data from the Seco Creek study area (Smith and others, 2003) and was developed in cooperation with Condor Consulting, Lakewood, Colorado.

Differencing two separate start/reference models was used to estimate the depth of investigation of the EM survey using the method described by Oldenburg and Li (1999). The two uniform start/reference conductivity values used were 0.001 and 0.004 S/m. Near the surface the conductivities defined by the two inversions are very similar, but at greater depths the conductivities diverge as the response becomes dominated by the reference model. The depth at which the calculated conductivities using the two reference models start to diverge significantly provides a measure of the depth of investigation (DOI).

A factor, *R*, was calculated to quantify the measure of divergence:

$$R = \text{ABS}(Cond_Refp004 - Cond_Refp001)/(Refp004 - Refp001)*100\%$$

where:

ABS is the absolute value function;

Cond_Refp004 is the conductivity of a layer calculated using reference model 0.004 S/m;

Cond_Refp001 is the conductivity of a layer calculated using reference model 0.001 S/m;

Refp004 is the conductivity of a first reference model: 0.004 S/m; and

Refp001 is the conductivity of the reference model 0.001 S/m.

The resistivity values (inverse of the conductivities) derived from inversion using reference model 0.004 S/m have been used in the presentations, but where the value of *R* (as defined above) exceeds 30 percent these layers have been nulled out, so that the bottom part of the section is blank. The depth to the bottom of the colored section represents the DOI. To some degree this is shallower in conductive areas because of the smaller skin depth and greater in the resistive areas due to the greater skin depth—but

mostly it appears controlled by the rate of drop-off of the signal amplitude with depth (cube of the depth below the RESOLVE bird). Skin depth is defined as the depth at which the signal amplitude is 1/e of the value at the surface, and functionally skin depth is inversely proportional to the square root of both frequency and conductivity.

4.0 PRESENTATION

4.1 MultiPlots

The results of the processing (profiles and RDIs) have been presented using Profile Analyst software (Encom Technology Pty. Ltd., 2008), with a horizontal scale of 1:24000 on 24"x36" plots. The horizontal X scale on every plot is in either UTM Easting or UTM Northing, depending on the angle of the flight line with true north. If this angle is less than or equal to 45°, then the UTM units are Northing; if this angle is greater than 45°, then the X coordinate represents Easting. A MultiPlot is a standard layout of HEM data and output on a single plotter sheet that was developed by Condor Consulting (written commun., 2004). The contents of a MultiPlot are described in the following section. A single example of a MultiPlot from Block B is shown in figure 2, and an example from Block D is shown in figure 3. Appendixes 1 and 2 contain the Multiplots for Block B and Block D, respectively.

4.2 Description of the MultiPlots

4.2.1 Panel 1 - Apparent Resistivities. This panel shows profiles of the pseudo-layer half-space apparent resistivities for the five coplanar coil pairs, as calculated and supplied by Fugro. Values are in ohm-meters and are plotted on a logarithmic vertical scale. The resistivity values differ for each frequency, as the lowest frequency has the greatest depth of penetration and the highest frequency has the least penetration.

4.2.2 Panel 2 – Powerline Monitor. The 60-Hz powerline channels for both coaxial and coplanar coils were recorded during the survey, and the coplanar 60-Hz signal is shown in this panel using a linear scale of 0-10 for Blocks B and D. The powerline monitor channel can be used as a diagnostic: anomalies in apparent resistivities coincident with spikes in this channel are subject to close evaluation for quality assurance.

4.2.3 Panel 3 – Differential Resistivity-Depth Section. This panel contains the resistivity sections based on differential parameters. The vertical axis is elevation above sea level in meters and has 400-m elevation span for Blocks B and D. Differential resistivity values at each coplanar frequency are plotted at the corresponding differential depth. The vertical depth extent is limited between the 100-kHz and 400-Hz differential depths with the remaining frequencies interpolated in between. The sections are not extrapolated to the surface resulting in the white, no-data area near the surface. The resistivities in the resistivity-depth section have been plotted using a stretched color scale to represent resistivity values, with a consistent range of 10-800 ohm-m for Blocks B and D. The topography is indicated by the black solid line. To enable easy recognition of how well

the helicopter has draped the topography, the height of the RESOLVE bird above the ground is indicated by the thin black-dotted-line profile above topography.

4.2.4 Panel 4 – Resistivity-Depth Section. This panel contains the RDI sections from the EM1DFM inversion. The resistivities in the resistivity-depth section have been plotted using the same vertical, horizontal, and color scales as in the differential depth sections. The bottom of the RDI sections have been truncated at the DOI, as discussed in section 3.0 above. To facilitate comparison with differential RDI (panel 3), the differential-depth at 400 Hz (the lowest operational frequency) is also plotted as a dotted black line below the inverted section. The height of the RESOLVE bird above the ground is indicated by the thin black-dotted-line profile above topography.

4.2.5 Panel 5 – Geological contacts and faults superimposed on 100-kHz apparent-resistivity grid. This shows a plan view of the apparent resistivity and superimposed geologic map features (same scale as the profiles) as a strip along the flight line, with the latter shown as the red line approximately centered in the panel. The purpose of this presentation is to enable quick and easy correlation of features observed on the profiles with geological features, and vice versa.

4.2.6 Panel 6 – Flight Line Index Map (top right of MultiPlot page). This shows (at small scale) all the lines of the survey, overlain on the 100-kHz apparent-resistivity grid with geologic contacts for reference. The current line displayed is highlighted in red, to indicate its location within the survey area.

5.0 STRUCTURAL AND GEOLOGIC INTERPRETATION

5.1 Faults and Geologic Contacts

The RDI (panel 4) of each flight line in each block was first compared to mapped geology by Ham and others, 1990 (panel 5). Three transitional categories were assigned, based on signatures evident in the geophysical data that correlated with the known geology: (1) major faults, which juxtapose fault blocks with extremely different electrical resistivities; (2) minor faults, which occur within a fault block and appear as subtle, but abrupt, electrical resistivity discontinuities; and (3) geologic contacts, which appear as subtle, gradual transitions between extensive areas of different, but consistent, electrical resistivities. Halihan and others (2008) have also analyzed the fracture and fault properties of the Arbuckle-Simpson aquifer. Their work could be integrated with the distribution of faults as interpreted from the HEM data.

Marker lines were placed along the RDI sections at each type of transitional category, as shown in figure 4. Then, in plan view, markers with definite correlation across adjacent flight lines were manually connected using bold solid lines for major faults, light solid lines for minor faults, and bold dashed lines for geologic contacts. Surveys flown as a suite of parallel lines impose an inherent limitation on this method. The signal contrast across a structural discontinuity, such as caused by a major fault between electrically distinct fault blocks, does not depend on the bearing of the HEM bird or the direction of

the flight line. The ability to locate the discontinuity on a map, however, is a function of spatial sample density. HEM data are acquired densely along the flight line, at roughly 8 to 10 meters per measurement. Data density perpendicular to flight lines depends on flight line spacing, which is driven by logistical and cost considerations. In the best case, the flight line intersects at a right angle and displays a sharp contrast at the discontinuity. In the worst case, the flight line runs parallel to the discontinuity, resulting in no abrupt change in signal contrast. Therefore, picks are readily discerned and more accurate when the flight line crosses a feature at an acute angle, whereas picks are more difficult and least accurate when the feature runs parallel between flight lines.

Block B encompasses the town of Ada's water supply wells and several springs, as shown in the base map in figure 5. The apparent resistivity map from the 100-kHz channel is shown in figure 6. High resistivities dominate the limestone areas with lower resistivities on the northeast flank.

The MultiPlot for a single flight line from Block B is shown in figure 2. Fence diagrams of the RDIs overlain on the previously mapped geology (Ham and others, 1990) are shown in figure 7. Whereas only a few faults were mapped in the limestone area, many are indicated on the northeast flank. Figure 8 shows the structural interpretation from the RDIs. Many minor faults are indicated in the limestone area, with the addition of a zone of faulting roughly parallel to the major fault demarcating the geology on the flank. This interpretation shows two of the town wells being intersected by fault structures. The complete set of Multiplots for Block B is given in appendix 1. General uniformity of geology characterizes this block with changes evident on the northeastern flank.

Block D is centered on the Spears Ranch well site (fig. 9). The survey area encompasses a cluster of springs and a major surface-water drainage. The apparent resistivity map from the 100-kHz channel (fig. 10) exhibits a gradual transition from high resistivities at the northwest to lower resistivities at the southeast.

The MultiPlot for a single flight line from Block D is shown in figure 3. Fence diagrams of the RDIs overlain on the previously mapped geology (Ham and others, 1990) are shown in figure 11, which shows faults converging at the cluster of springs. Figure 12 shows the new structural interpretation derived from the RDIs. More, but less continuous faults are indicated, with no extensive faulting at the cluster of springs. More geologic contacts are seen in the southeast, which may indicate a more varied limestone composition. A difference in composition of the rocks in this portion of the survey area could explain the observed lower electrical resistivities. The complete set of Multiplots for Block D is given in Appendix 2. The geology is generally uniform (Arbuckle Group rocks), with only a few distinctive features.

In the final analysis, the geophysical interpretations of Blocks B and D should be integrated with a reinterpretation of the structural geology by a structural geologist familiar with structural styles in the Arbuckle anticline. The reinterpretation of the geology would be facilitated by new geologic mapping of critical areas identified by the airborne geophysical interpretation given here.

Smith and others (2007), Smith, Blome, and others (2008), and Smith, Smith, Blome, and Osborn (2008) have compared the results of the HEM RDI with ground electrical resistivity imaging (ERI) surveys, as have Riley (2004), Halihan and others (2004), and Sample (2008). The comparison between ground and airborne RDI is very good (fig. 13). In general the ground resistivity survey has greater detail, which is no surprise given that electrode spacings are much smaller than the airborne EM footprint. The resolution of high resistivities (above 2000 ohm-m) is better with a galvanic ground system than an induction system. In general the color scale used in the presentations of the HEM data and the RDI sections along flight lines does not have as high a resistivity as scales used for the ground surveys.

The general patterns of resistivity from the apparent resistivity maps and the RDI sections suggest that the Arbuckle Group has higher resistivities than the Simpson Group. Also the Kindblade Formation within the Arbuckle Group has a higher overall resistivity than the West Spring Creek Formation, which shows more areas having moderate resistivities. These general observations can be used in further geologic mapping within the HEM flight areas.

5.2 Epikarst and Soil

For the purpose of this report, epikarst refers to a portion of the bedrock that extends from the base of the soil zone and is characterized by extreme fracturing and enhanced solution (Field, 1999). Soil developed in response to in place weathering in karst terrains is frequently referred to as a residuum (Gamey and others, 2002). Epikarst is characterized by fractures and solution pockets that may or may not be filled with water. Epikarst in general is thought to be important in the near-surface hydrology of carbonate terrains (Klimchouk, 2004).

An airborne geophysical survey, similar to the one reported here, was carried out in Missouri over an area of epikarst and residuum (Gamey and others, 2002). The goal of that study was to map possible flow paths for contaminants in a well-developed, thick residuum. Epikarst, though recognized in the Hunton anticline, has not been consistently mapped. The Oklahoma Water Resources Board funded a study by Sample (2008) to characterize the geophysical, hydrologic, and geologic parameters of epikarst in the Hunton anticline in specific study areas.

The above studies have shown electrical resistivity of epikarst is typically lower than that of the source bedrock, due in part to higher concentrations of fine-grained residual material, such as clay. As a result, occurrences of epikarst are mapped as a low resistivity layer overlying higher resistivity country rock, in particular limestone and dolomite. Likewise, soils would exhibit a lower resistivity owing to relatively higher water or clay content. Thus, both epikarst and soil present similar HEM signatures with the major difference being the thickness. Soils appear as a veneer over bedrock or over epikarst.

The basic groundwater issue related to the soil, residuum, and epikarst is its significance for potential water storage and recharge to the bedrock. As in the study by Gamey and others (2002), the residuum also is a control on near-surface water flow paths. Sample (2008) concluded that the storage potential for these units was the same order of magnitude as the saturated thickness of the aquifer itself. The HEM survey offers critical data that can be used to map the extent of these units in the area of the Arbuckle-Simpson aquifers.

Three sites that Sample (2008) studied with ERI, soil penetrometer, and other methods are near HEM survey areas: (1) Hatch area west of Block B, (2) Arbuckle Simpson Ranch (ARS) in Block D, and (3) Spears Ranch Well (SRW) site in Block D. The Hatch area is not discussed in detail here since it is not within the airborne survey area. The ERI transects are shown as short red-line segments in the Block D base map (fig. 9).

The part of Block D that contains ground ERI surveys is shown in figure 14A. The airborne HEM survey apparent resistivity map (fig. 10) show that the northwest part of Block D has a higher apparent resistivity than the southeast part. Mapped structures and those interpreted from the HEM (fig. 12) described above would generally be expected to influence the depth and extent of epikarst development (Klimchouk, 2004). The two ground profiles are located near one HEM line (L40050). The RDI shown in figure 14B along the HEM flight line that is near both ground surveys indicates that the bedrock is more resistive in the northeast part of the survey area. Note that the color scale for the HEM in figure 14B has been chosen to match the color scale used by Sample (2008) for the ERI images. In general the major fault (fiducial 714490 Easting on fig.14B) is associated with a zone of lower resistivity that extends to depth of at least 60 m that could indicate a thickening of the epikarst over a possible buried karstic feature. This is certainly an area where enhanced recharge or groundwater flow may occur.

The ERI line at the SRW site shows that no high resistivity (greater than 500 ohm-m) bedrock is within the depth range of the survey (fig. 14C). However, the geologic map for this part of Block D does not show a change in basement geology (Arbuckle Group). The general comparison between the ERI depth section and the HEM depth section (fig. 14C and 14D) is good with both mapping lower resistivity in the SRW site. The ground profiles generally have a greater and higher range of resistivity than the airborne RDIs. Sample (2008) noted in general that direct-push electrical conductivity (EC) probe measurements were higher by at least a factor of two than the ground ERI survey values. Thus, part of the reason for the difference in resistivity range is a difference in the volume of ground sampled for the different techniques. The EC technique samples the smallest volume, the ERI senses a larger volume, and the airborne survey samples the largest.

Figures 14C and 14D show the airborne and ground RDI at the same general scale with the interpreted depth of the epikarst from Sample (2008). This particular ERI site is anomalous in that there is no resistive (more than 500 ohm-m) bedrock within the depth of investigation. If bedrock is within range of the geophysics, then it is not resistive limestones but a lower resistivity lithology such as silty sandstones or limestone. Since

there is not a great electrical contrast between epikarst and bedrock, Sample (2008) relied heavily on penetrometer data. We have shown the HEM RDI with a different color scale in Figure 14D, which emphasizes the surface lower resistivity unit. This unit correlates generally well with the depth estimated by Sample (2008).

In our treatment of soil/epikarst signatures, we analyzed shallow (less than 10 m) resistivity variations in the RDIs. Generally the epikarst has a markedly lower resistivity in comparison to the bedrock at the Arbuckle Spears Ranch in both the ground and airborne RDI. Thin, low resistivity layers overlying more resistive limestone were demarcated using white-filled rectangles, whose lengths equaled the lengths of the soil/epikarst signatures, as shown in figure 15. Areas devoid of the low resistivity layer were left blank. The set of these rectangles in a survey area were connected across individual survey lines wherever adjacent lines had proximate rectangles. A maps were made showing the coverage of epikarst/soil in Block B (fig. 16) and in Block D (fig. 17). Areas with epikarst/soil are stippled, whereas thin soil/bedrock outcrops are blank.

6.0 CONCLUSIONS

HEM data from Blocks B and D in the Hunton anticline were intensively analyzed. First, the data were inverted to give resistivity depth inversion profiles. Then, individual RDIs were closely examined to yield picks for geologic structure, geologic contacts, and occurrence of epikarst. Based upon the picks, maps were created of interpreted structure, contacts, and epikarst. The HEM results were corroborated using the analysis and interpretation of ERI surveys performed independently by Oklahoma State University investigators.

In Block B, the picked faults show similarity to mapped faults only in the northeastern portion, which lies on the flank of the anticline. Evidently, the core limestone rocks do not have sufficiently different electrical properties across faults to manifest as a discontinuity in the HEM data. It is interesting that two of the three Ada wells are intersected by picked faults, whereas in the mapped faults, only one well is sited on a fault.

In Block D, some of the picked faults roughly correlate with mapped faults in the northwest-central and southeast portions of the survey area. As with Block B, the limestone rocks apparently do not have sufficiently different electrical properties across the mapped faults to cause distinct anomalies in the HEM data.

The HEM data effectively maps the soil and epikarst. Though the resolution of these features is less than the ground ERI surveys, they correlate well. Both surveys suggest that the epikarst is extensive. The extent of the epikarst/soil has been interpreted for survey Blocks B and D. The epikarst has not been previously mapped. Consequently, new geologic mapping should include epikarst since it appears to be a significant component of the hydrogeologic setting.

7.0 REFERENCES

Condor Consulting, Inc., 2003, Processing report: EM1DFM inversions of DIGHEM data from the Seco Creek Area, Texas. Unpublished report.

Encom Technology Party Ltd., 2008, Users Guide, Profile Analyst Version 8, North Sydney, Australia, 174 p.

Farquharson, C.G., and Oldenburg, D.W., 2004, A comparison of automatic techniques for estimating the regularization parameter in nonlinear inverse problems, *Geophysical Journal International*, 156, p. 11-425.

Farquharson, C.G. and Oldenburg, D.W., 2000, Automatic estimation of the tradeoff parameter in nonlinear inverse problems using the GCV and L-curve criteria: SEG 70th Annual Meeting, Calgary, Alberta, 6-11 August, 2000.

Field, M.S., 1999, A lexicon of cave and karst terminology with special reference to environmental karst hydrology: U.S. Environmental Protection Agency, National Center for Environmental Assessment, EPA/600/R-99/006, 201 p. Digital version by Karst Waters Institute.

Fraser, D., 1978, Resistivity mapping with an airborne multicoil electromagnetic system: *Geophysics*, v. 43, p.144-172.

Fugro Airborne Surveys, <http://www.fugroairborne.com/service/resolve.php> (valid on 02/23/09).

Gamey, T.J., Thompson, M., Mandell, W., Frano, G., and Miller, S., 2002, Karst pathway delineation using combined spatial and geophysical analysis at Camp Crowder, Missouri: Proceedings for the 15th Symposium on the Application of Geophysics to Environmental and Engineering Problems, 12 p.

Halihan, T, Paxton, S., Puckette, J., Sample, M. 2004, Preliminary electrical resistivity imaging report for: The Arbuckle-Simpson Hydrology Study: report submitted to the Oklahoma Water Resources Board, 27 p.

Halihan, T., Mouri, S., Puckette, J., 2008, Evaluation of Fracture Properties of the Arbuckle-Simpson Aquifer, Oklahoma State University School of Geology, report to the Oklahoma Water Resources Board.

Ham, W.E., McKinley, M.E., and others, 1954, revised by Johnson, K.S., 1990, Geologic map and sections of the Arbuckle Mountains, Oklahoma, *in* Hydrology of the Arbuckle Mountains area, south-central Oklahoma: Oklahoma Geological Survey, Circular 91, Plate 1.

Huang, H., and Fraser, D.C., 1996, The differential parameter method for multifrequency airborne resistivity mapping: *Geophysics*, 61, p. 100-109.

Klimchouk, A., 2004, Towards defining and delimiting and classifying epikarst: Its origin, and variants of geomorphic evolution, *in* W.K. Jones, Culver, D.C., and Herman, J., eds., *Karst Waters Institute Special Publication*, v. 9, p. 13-35, republished (modified), 2004, in *Speleogenesis and Evolution of Karst Waters*, v. 2, no. 1, p. 1-13.

Oldenburg, D.W., and Li, Y., 1999, Estimating depth of investigation in DC resistivity and IP surveys. *Geophysics* 64, 2, p. 403-416.

Riley, M.E., 2004, Investigation of fault properties using electrical resistivity imaging: Master of Science Thesis, Oklahoma State University, Norman, Oklahoma, 104 p.

Sample, M.S., 2008, Characterization of the epikarst over the Hunton anticline, Arbuckle-Simpson aquifer, Oklahoma: M.S. Thesis, Oklahoma State University, 220 p.

Smith, B.D., Irvine, R., Blome, C.D., Clark, A.K., and Smith, D.V., 2003, Preliminary results, helicopter electromagnetic and magnetic survey of the Seco Creek area, Medina and Uvalde Counties, Texas: Proceedings for the Symposium on the Application of Geophysics to Environmental and Engineering Problems, San Antonio, Texas, 13 p.

Smith, B.D., Blome, C.D., Smith, D.V., Scheirer, D.D., Deszcz-Pan, M., 2008, Geophysical surveys to characterize the hydrogeology of the Arbuckle uplift, south-central Oklahoma: Symposium on Environmental and Engineering Geophysics, Annual Meeting Proceedings, Philadelphia, Pennsylvania, p. 539-548.

Smith, B.D., Smith, D.V., and Blome, C.D., 2008, Helicopter electromagnetic surveys of carbonate karstic aquifers with emphasis on recent applications by the U.S. Geological Survey: 5th International Conference on Airborne Electromagnetics, Haikko Manor, Finland, 4 p.

Smith, D.V., Smith, B.D., Blome, C.D., Halihan, T., Back, J., 2007, Preliminary results of airborne and ground resistivity surveys for subsurface mapping in the Hunton anticline, south-central Oklahoma: Geological Society of America Annual Meeting, Denver, Colorado, 1 p.

Smith, D.V., Smith, B.D., Blome, C.D., and Osborn, N., 2008, Airborne and ground electrical surveys for subsurface mapping of the Arbuckle aquifer, central Oklahoma: American Geophysical Union Annual Meeting, San Francisco, California, 1 p.

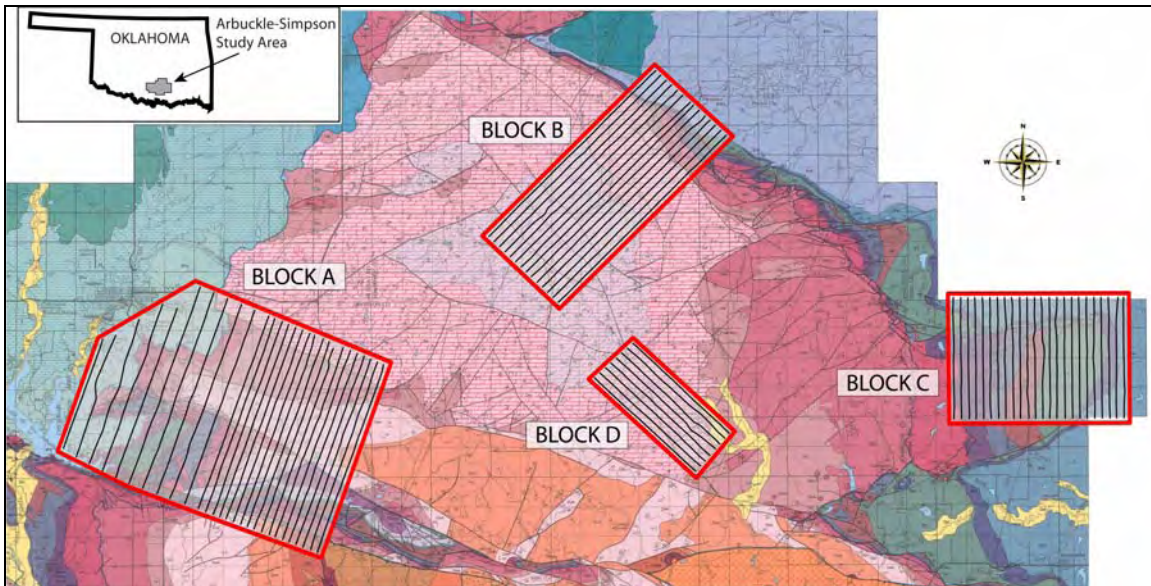


Figure 1. Index Map of Helicopter EM Survey Blocks (map adapted from Ham and others, 1990).

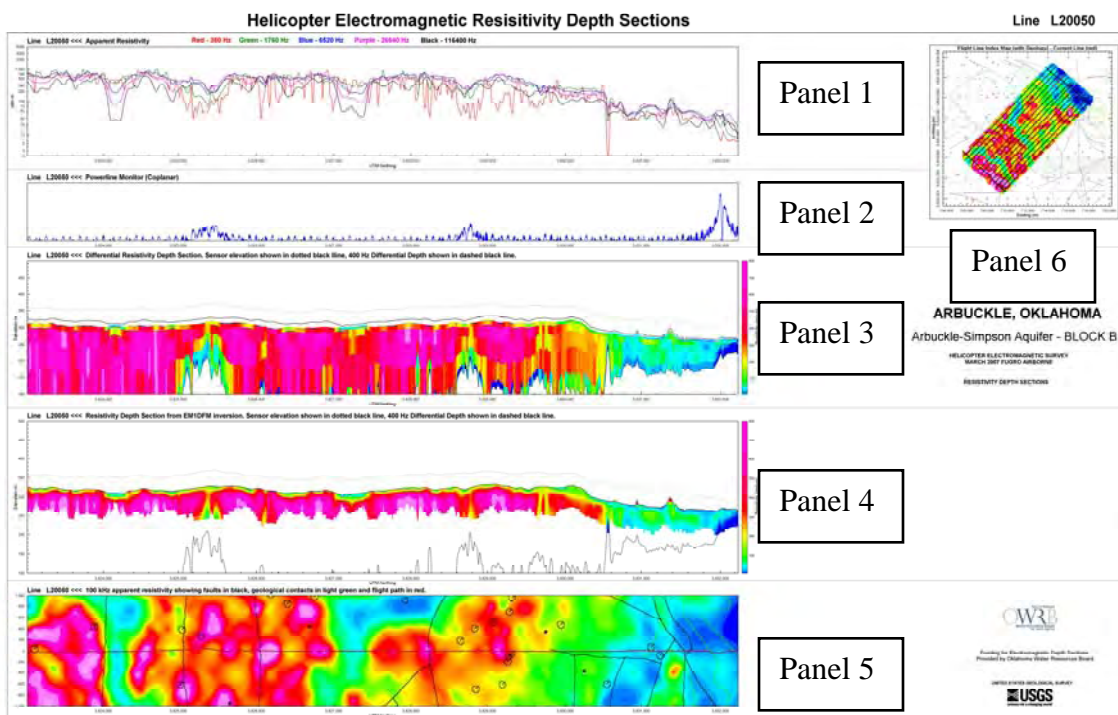


Figure 2. MultiPlot showing a representative example of flight line data, RDIs, and apparent resistivity map from Block B (see text for additional description).

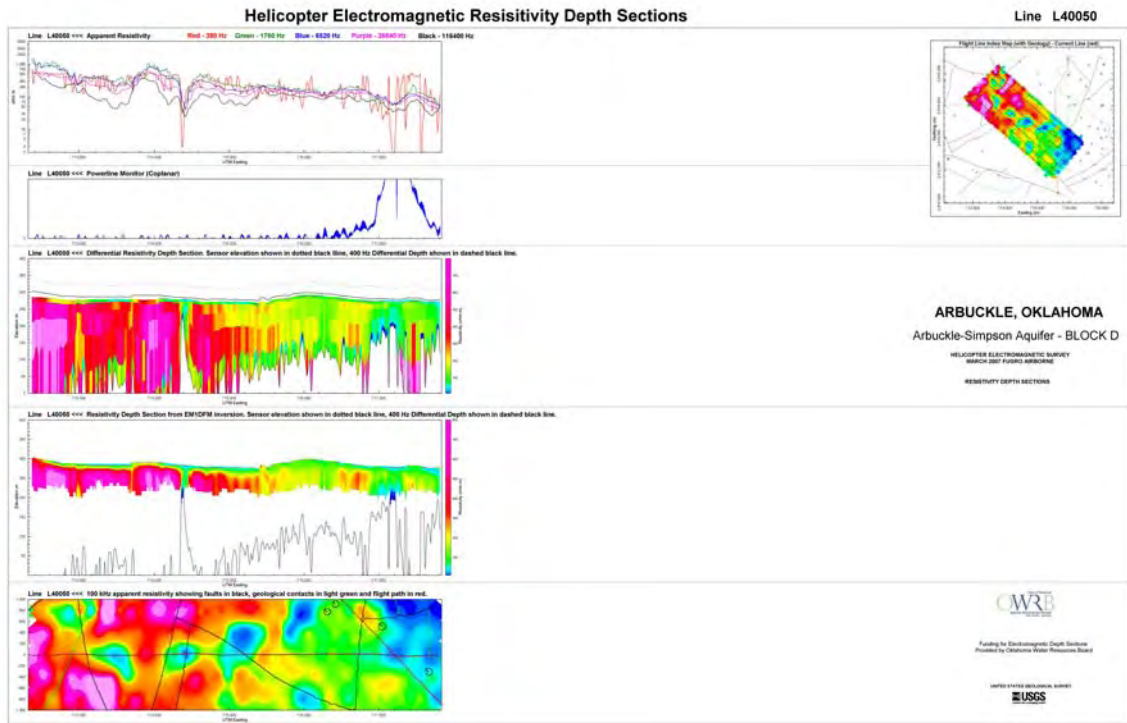


Figure 3. MultiPlot showing a representative example of flight line data, RDIs, and apparent resistivity map from Block D (see text for additional description).

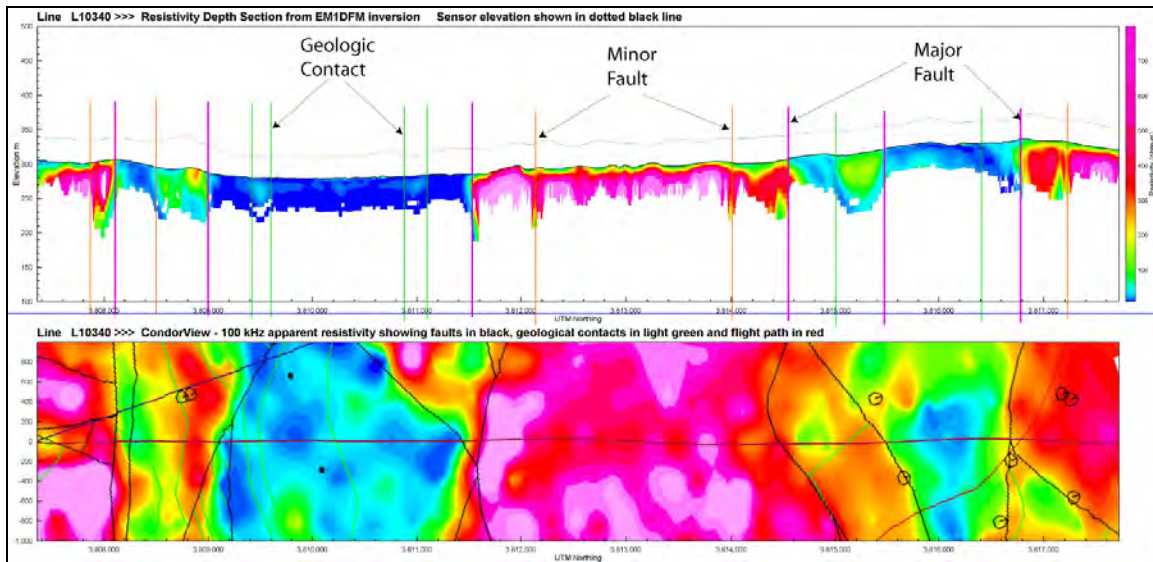


Figure 4 . Example of interpreted features picked on an RDI (upper plot) with distinctive markers (note map and RDI have different color scale).

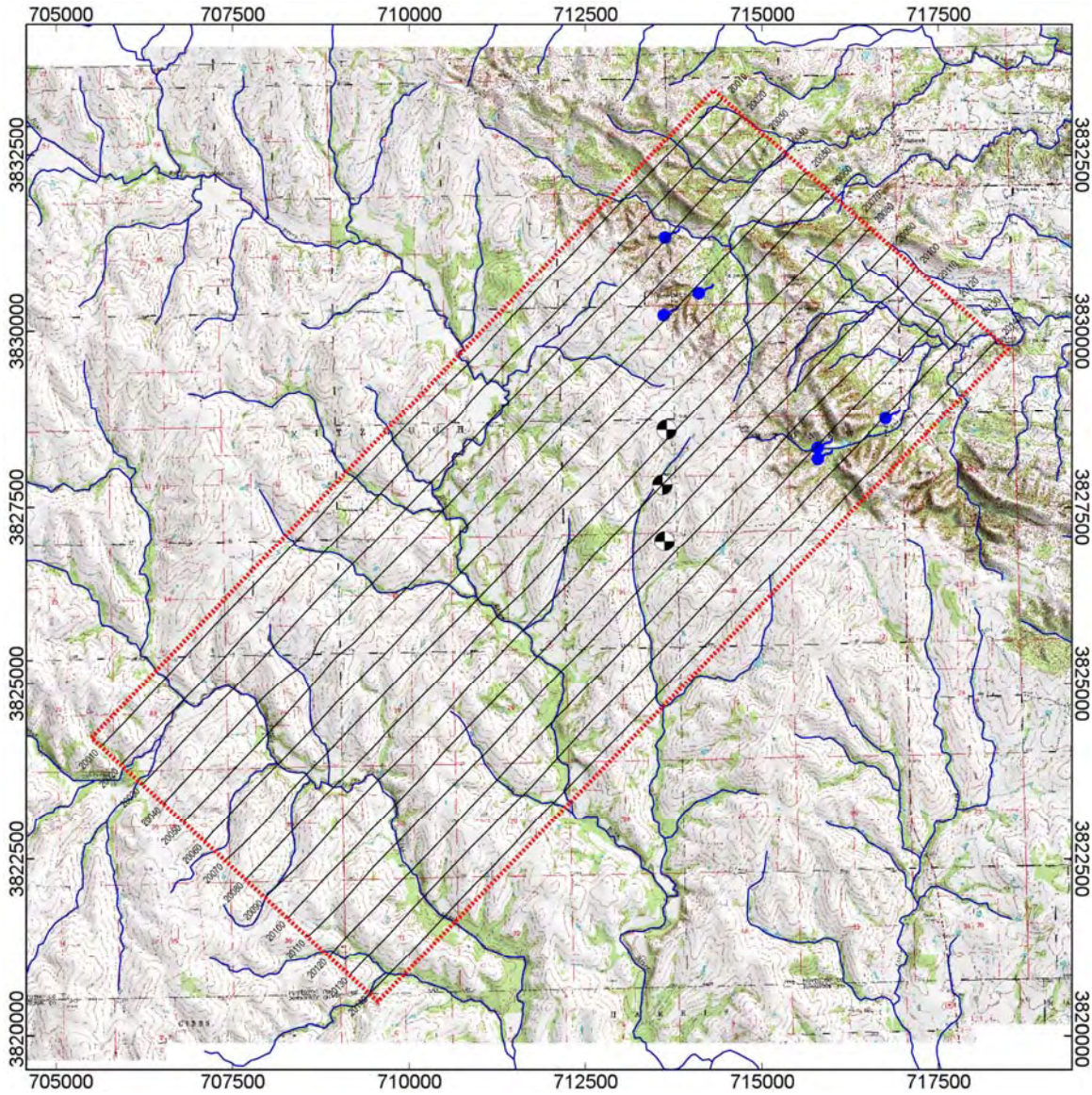


Figure 5. Block B base map showing flight lines (black), drainages (blue lines), springs (blue dots), and the city of Ada's water supply wells (disks).

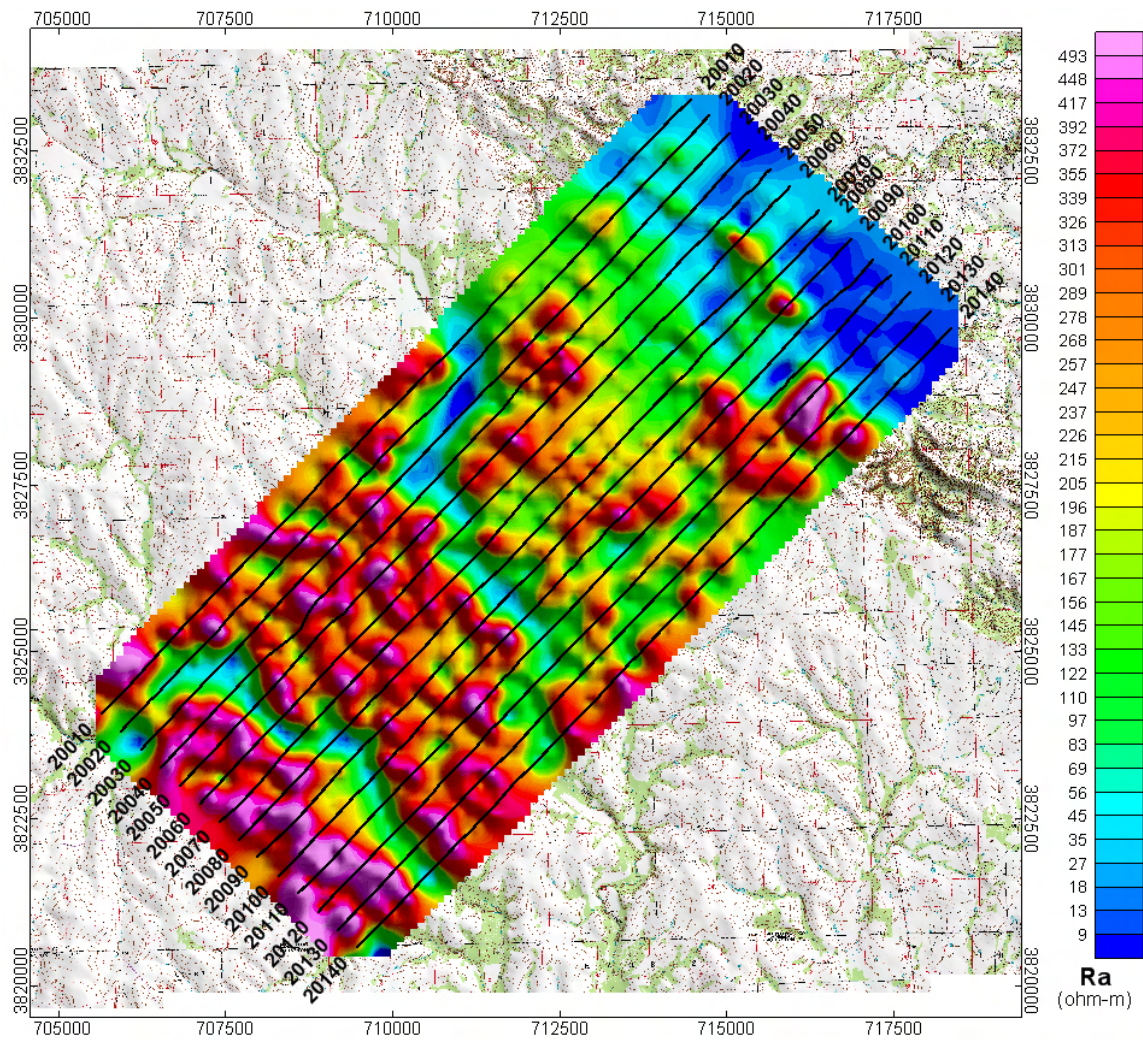


Figure 6. Apparent resistivity map for Block B of the 100-kHz channel with flight lines (black) shown (high resistivities are in warmer colors).

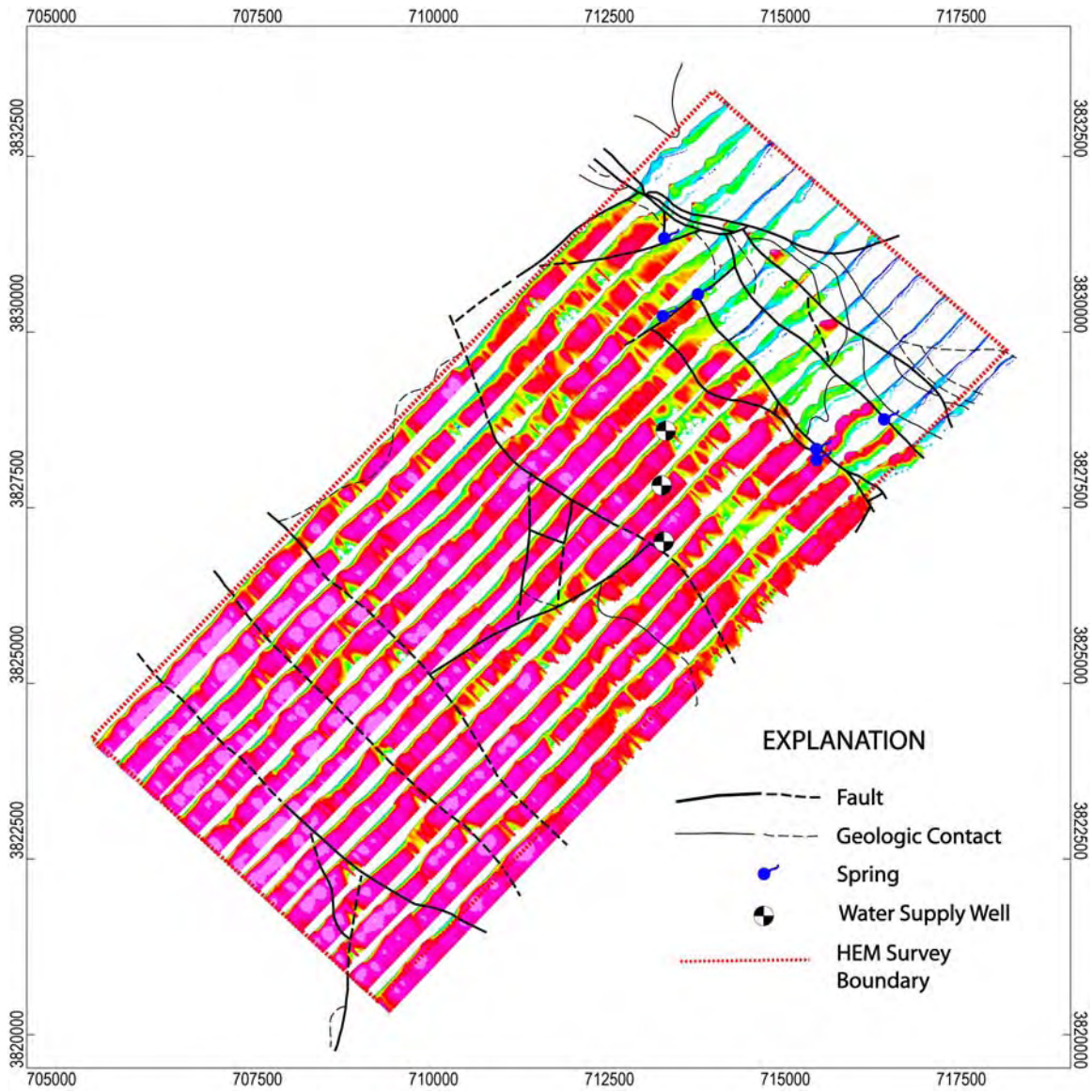


Figure 7. Structure (adapted from Ham and others, 1990) superimposed on fence diagram of RDIs.

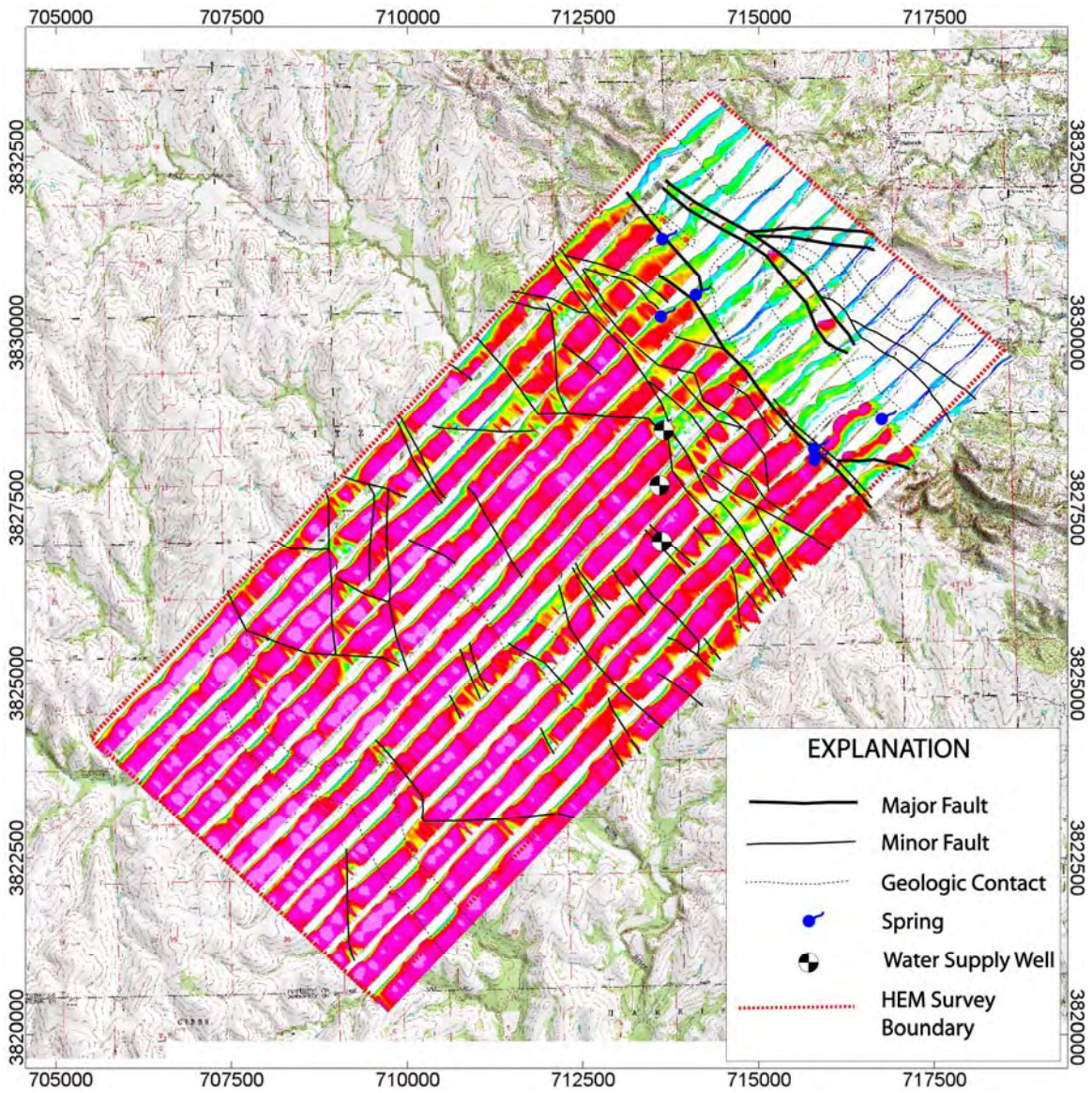


Figure 8. Structure interpreted from the HEM survey superimposed on fence diagram of RDIs.

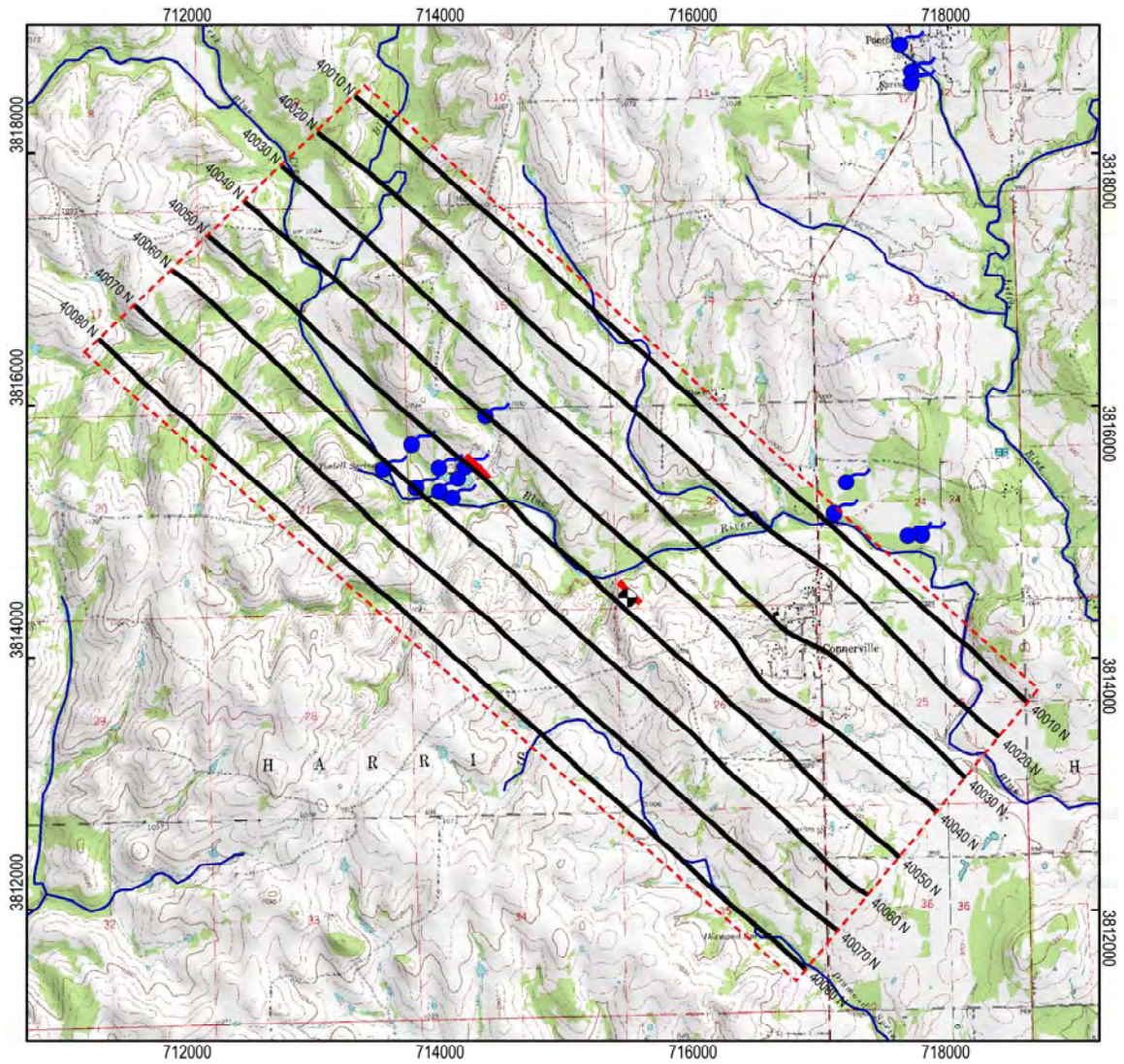


Figure 9. Block D base map showing flight lines (black), drainages (blue lines), springs (blue dots), the Spears Ranch exploratory well (disk), and the two ERI transects (red).

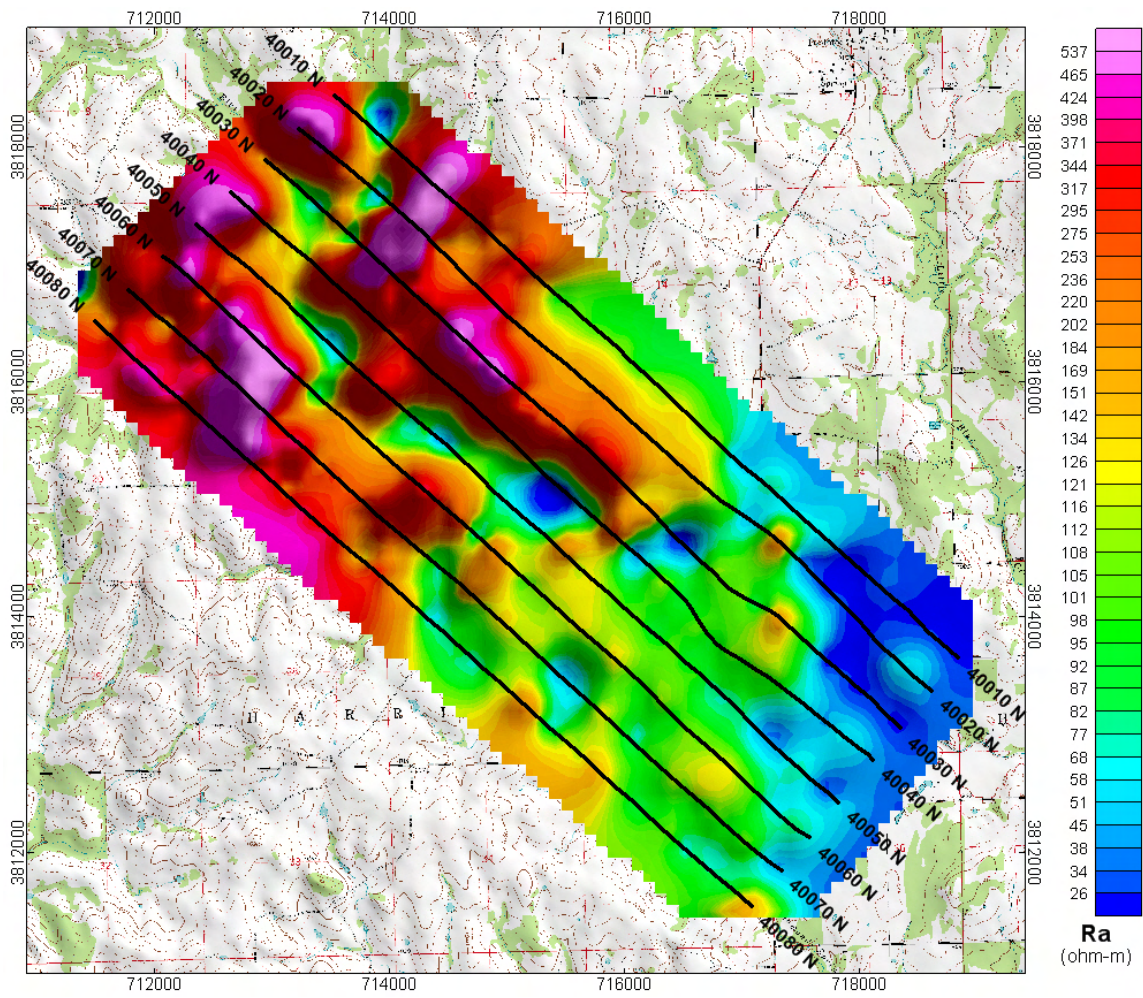


Figure 10. Apparent resistivity map of Block D for the 100-kHz channel with flight lines (dark lines with numbers).

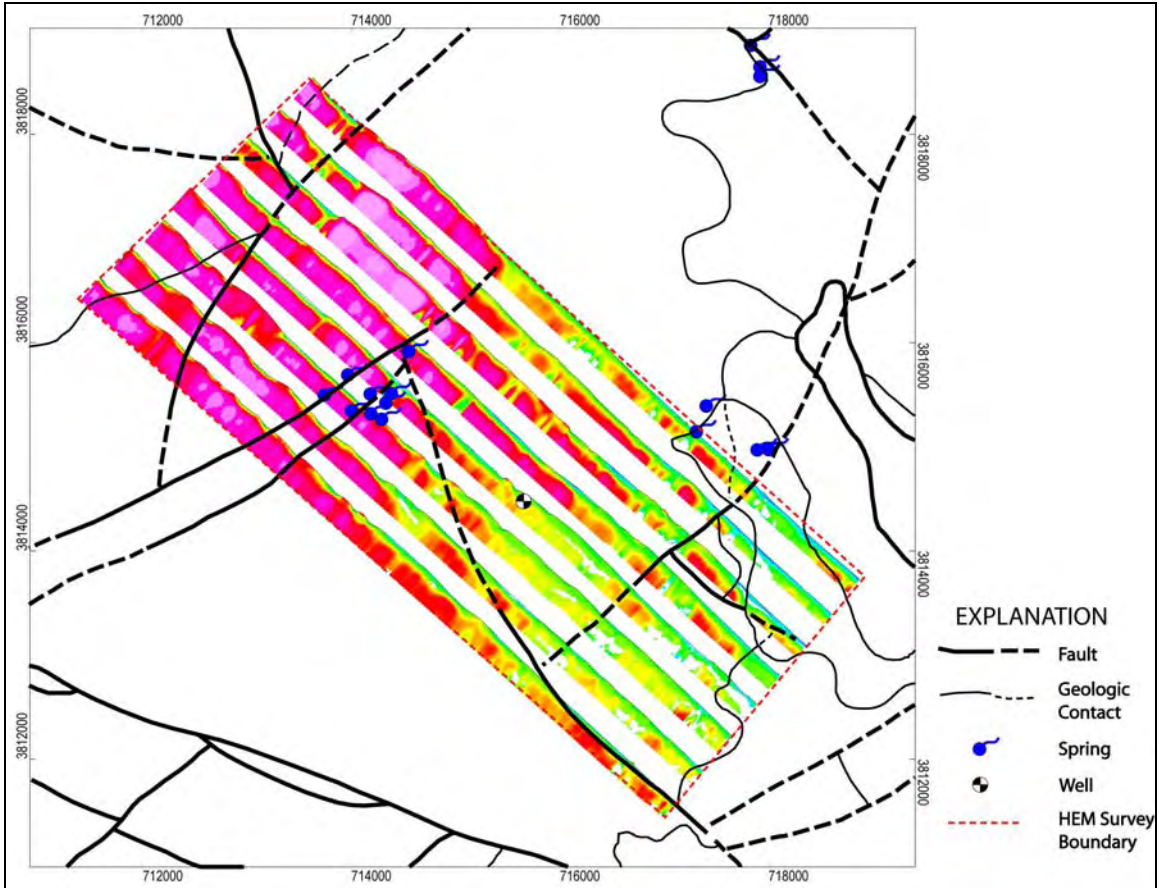


Figure 11. Block D fence diagram of RDIs with previously mapped geology (adapted from Ham and others, 1990).

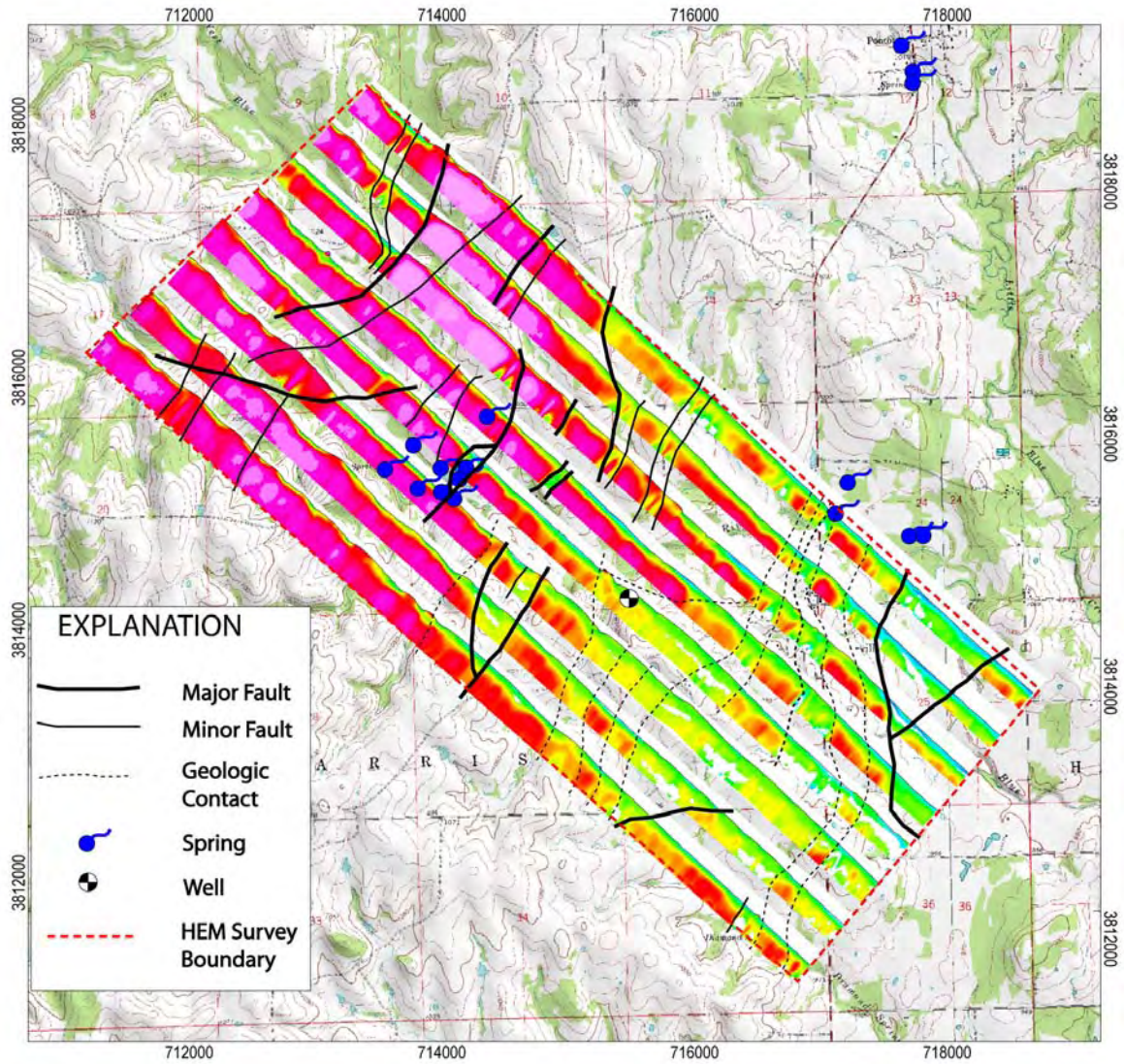


Figure 12. Block D fence diagram of RDIs with interpreted geologic structure with topographic features in the background.

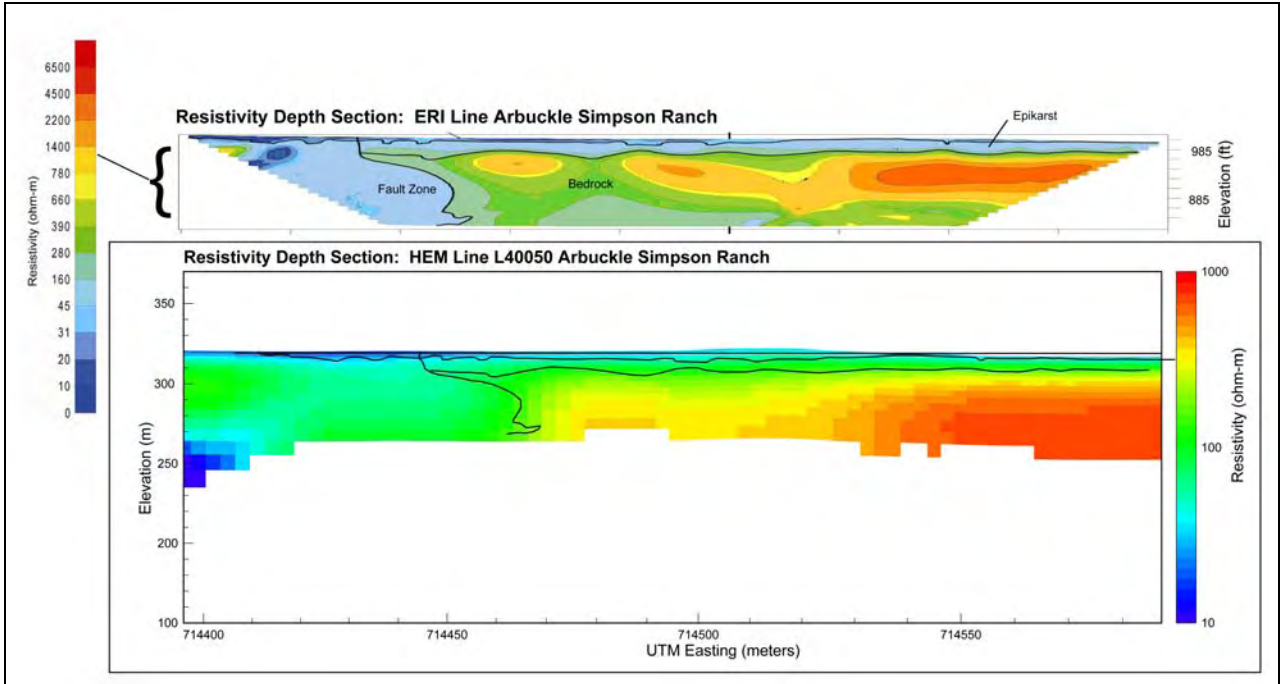


Figure 13. Ground electrical resistivity line at the Arbuckle Simpson Ranch site (top profile, Sample, 2008) is shown at the same vertical and horizontal scale as the airborne resistivity depth image along line L40050 (bottom profile). The interpreted units from the ground survey are shown superimposed on the airborne depth image. Note that the resistivity color scales for each depth section are different (see text for discussion).

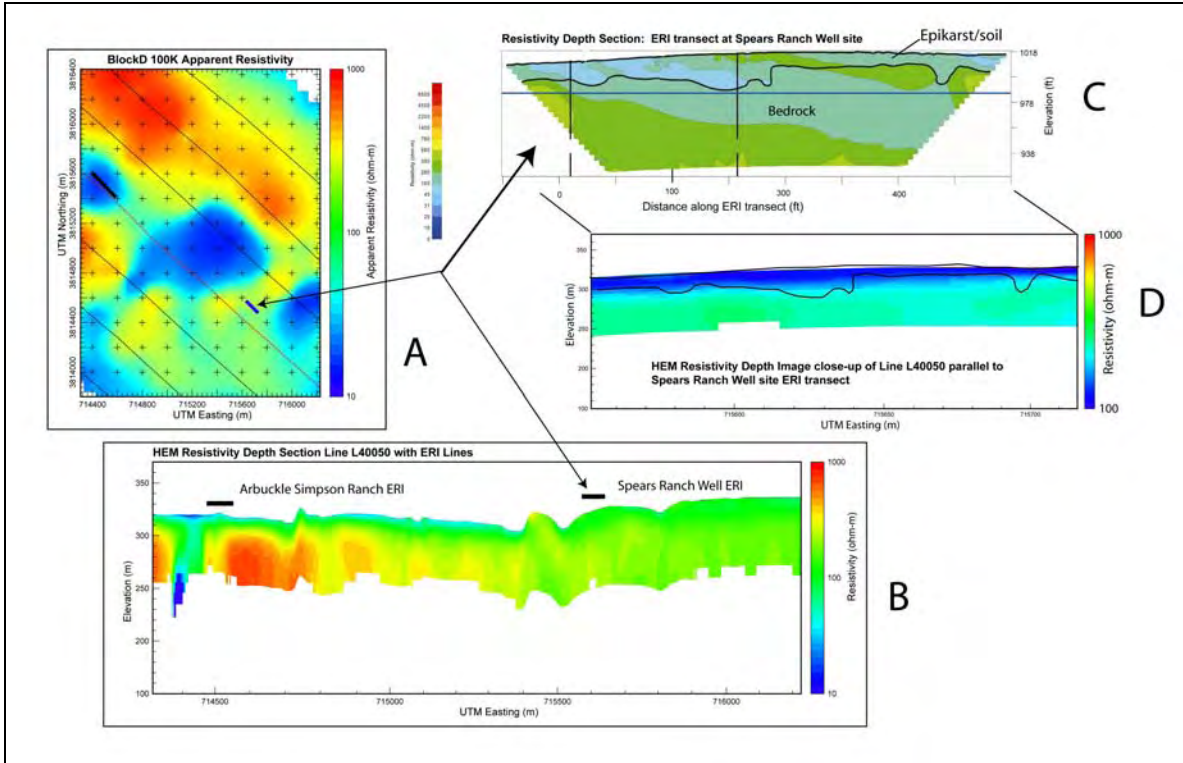


Figure 14. HEM resistivity depth image (RDI) along line L40050 showing the location of ERI transects at the Arbuckle Simpson Ranch site and the Spears Ranch well site. Map view (A) showing flight lines and ground profile lines on the 100-kHz apparent resistivity map. The HEM RDI for the entire line is shown in (B) with the locations of the ground profiles. The ERI profile for the Spears Ranch well site is shown in (C). An enlargement of the HEM profile (B) is shown in (D) at the same horizontal scale as the ERI line and with the interpreted depth of epikarst from direct-push penetrometer data. The HEM RDI is the projected length of the true ground RDI profile 200 m northeast of the HEM flight line (red line in A). Note that the resistivity color scales for apparent resistivity map and the depth section are different (see text for discussion).

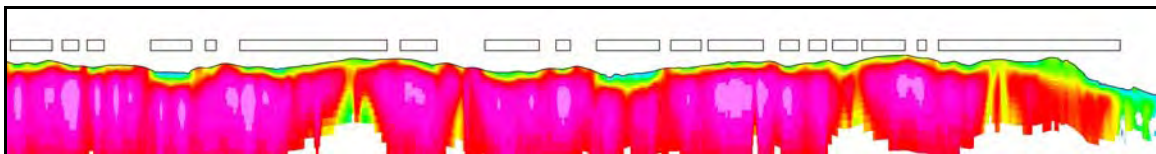


Figure 15. White boxes correspond to zones of epikarst or soil (green) overlying limestone (red) inferred from the underlying RDI.

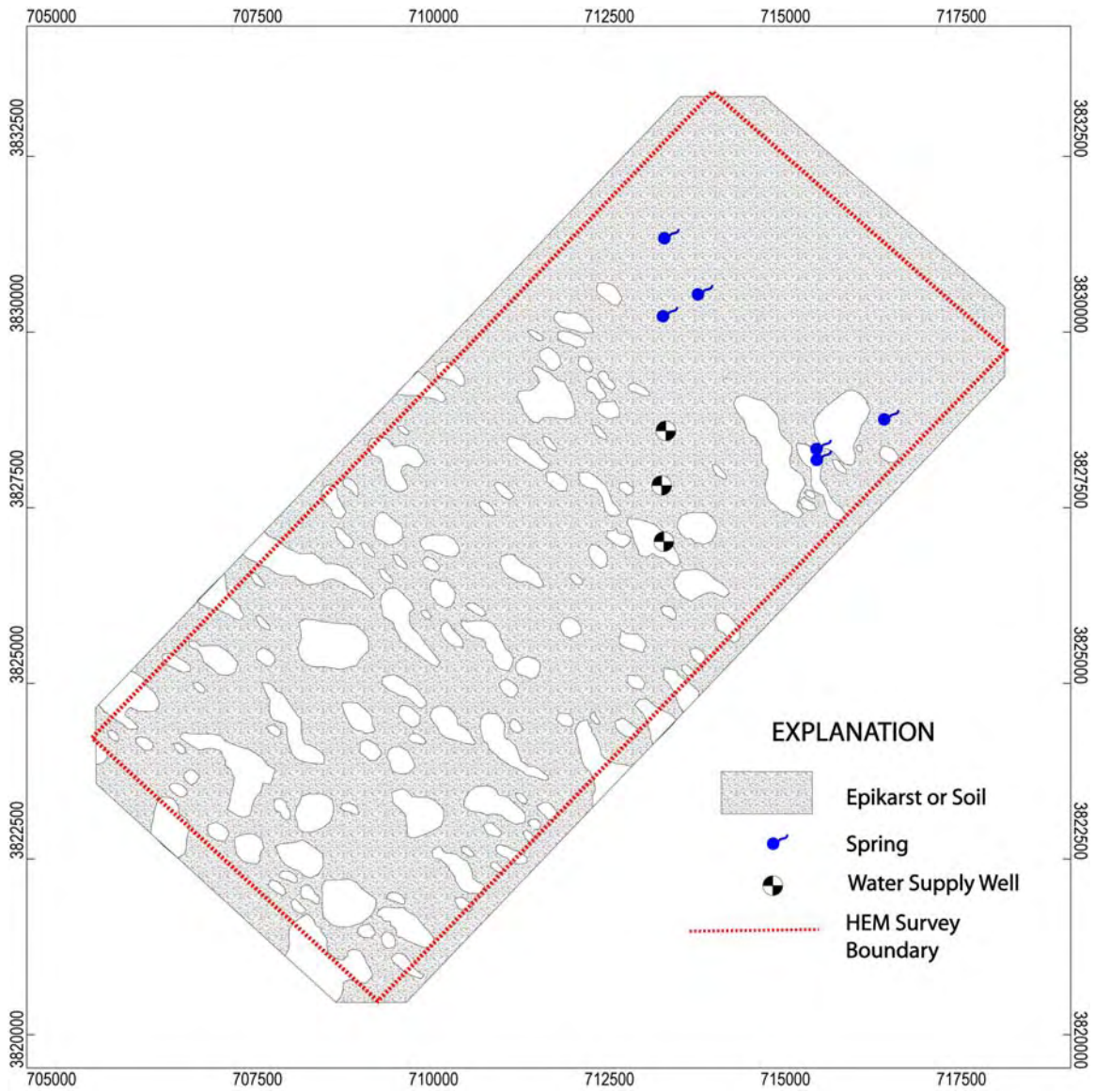


Figure 16. Map of epikarst or soil occurrence for Block B.

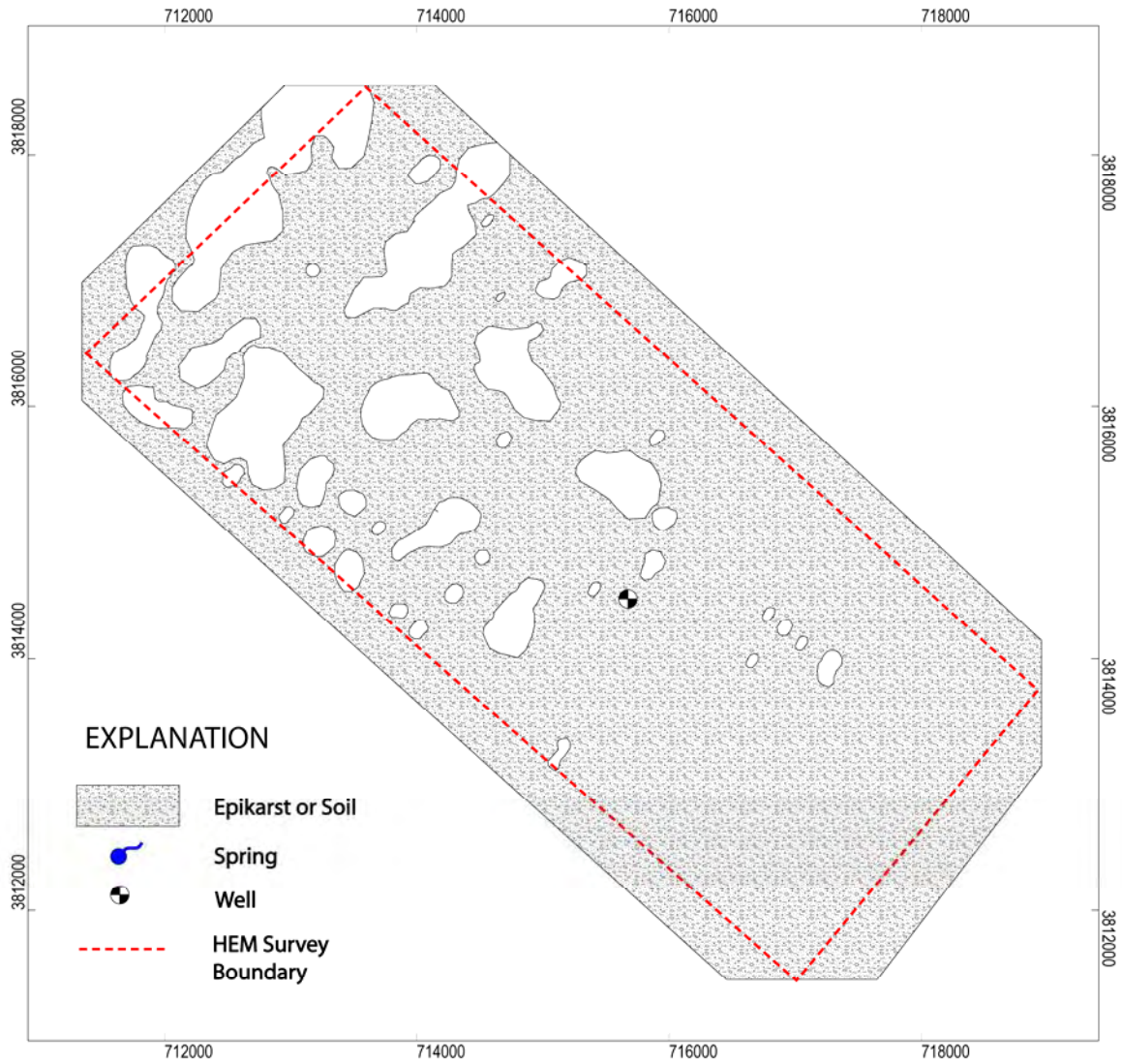


Figure 17. Block D map of interpreted epikarst/soil distribution.

Appendix 1. Block B MultiPlots

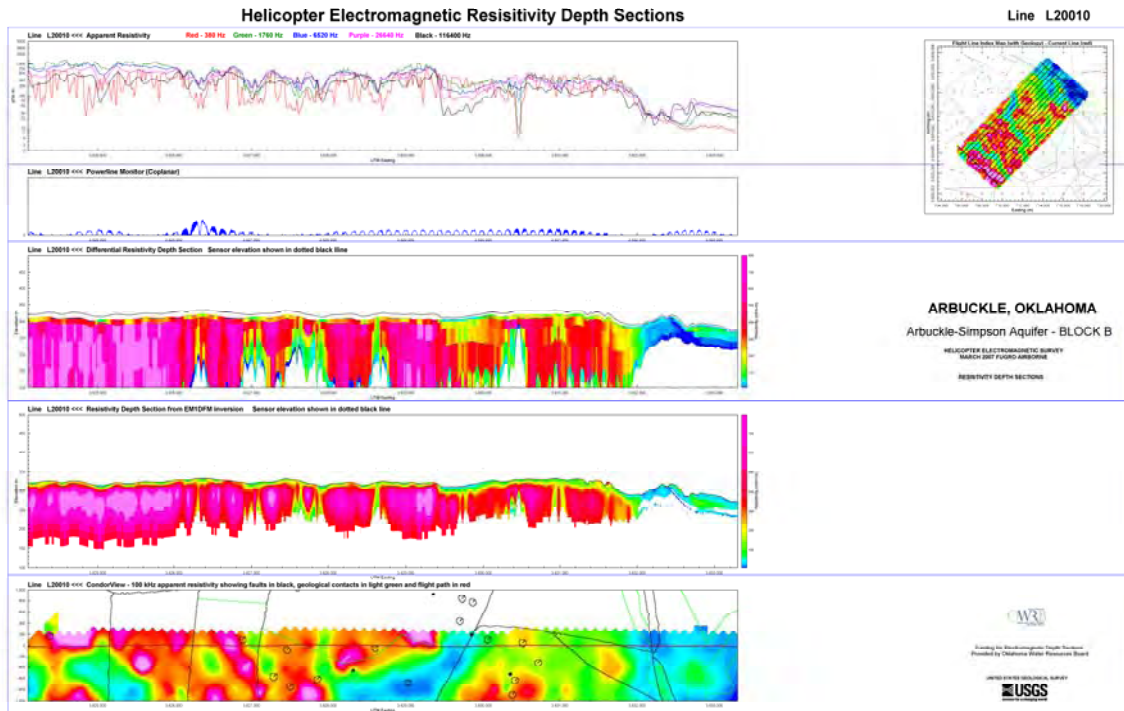


Figure A1-1. Block B Line L20010

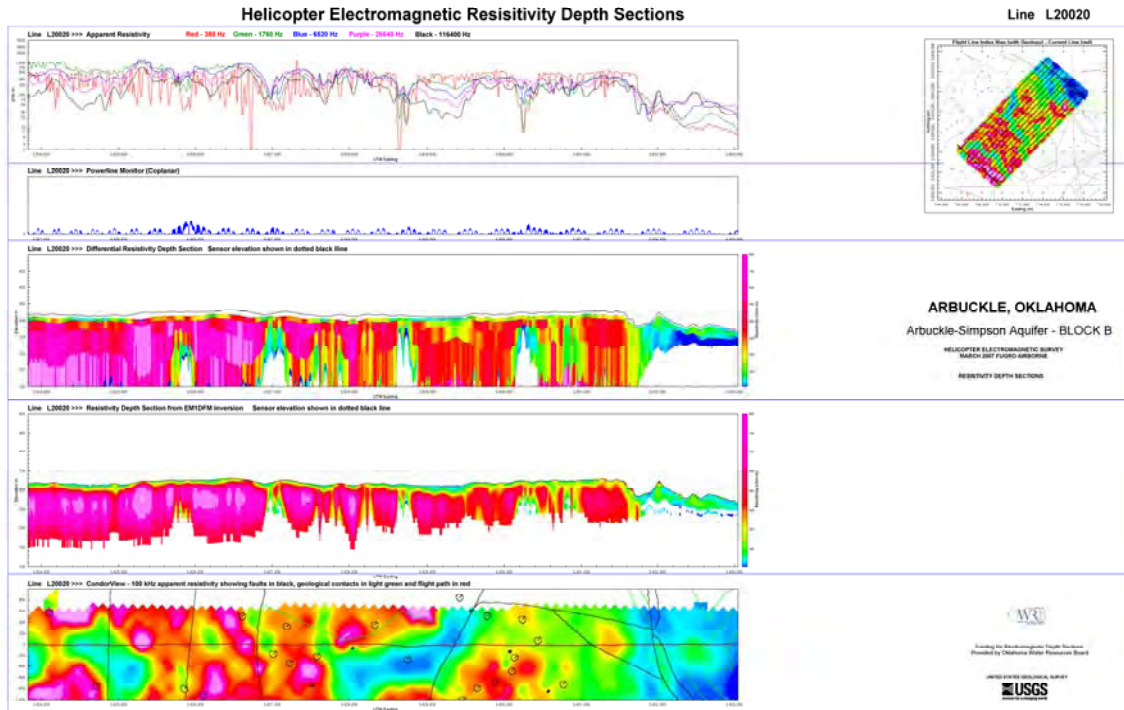


Figure A1-2. Block B Line L20020

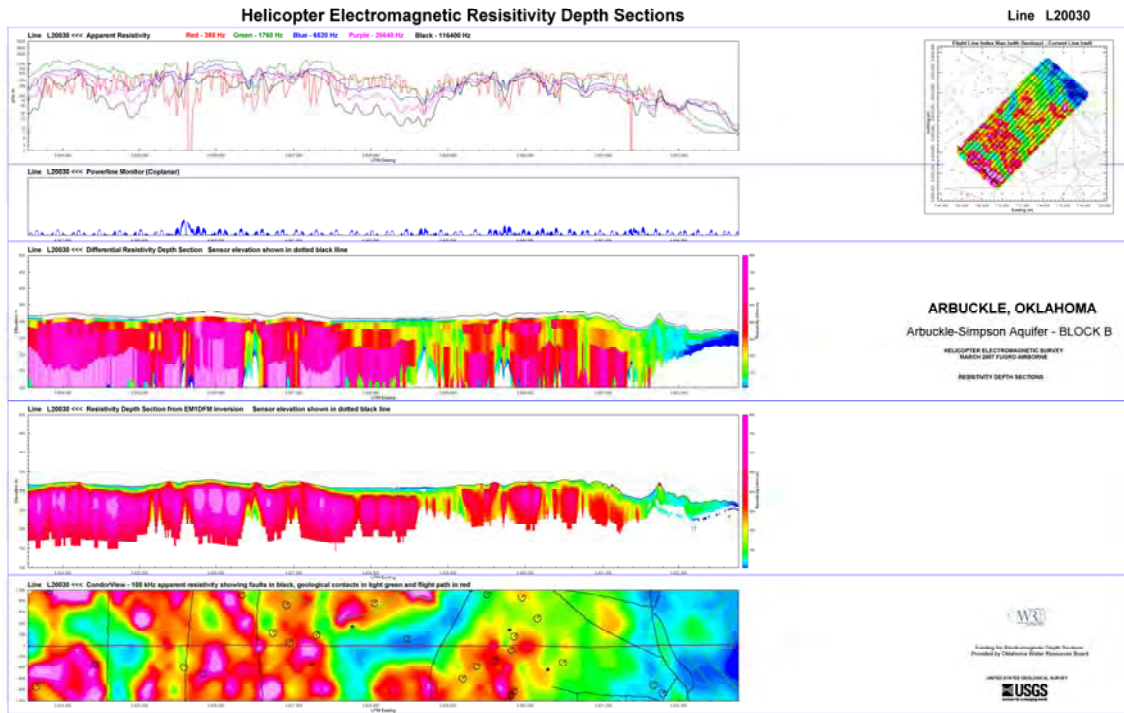


Figure A1-3. Block B Line L20030

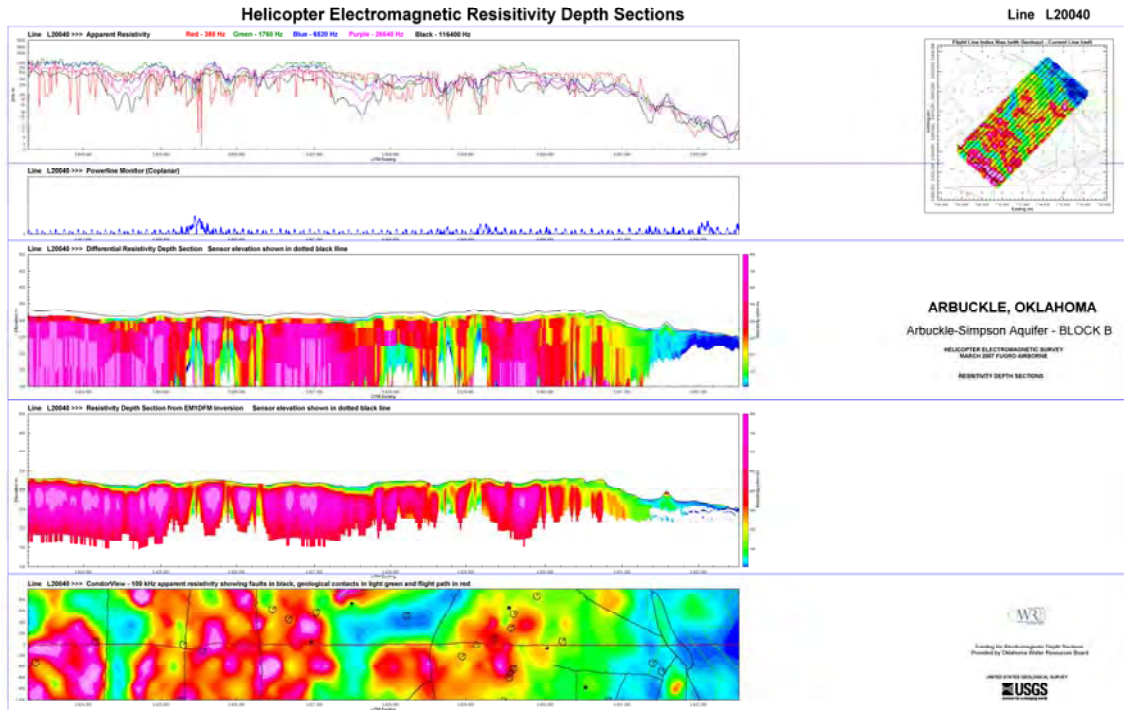


Figure A1-4. Block B Line L20040

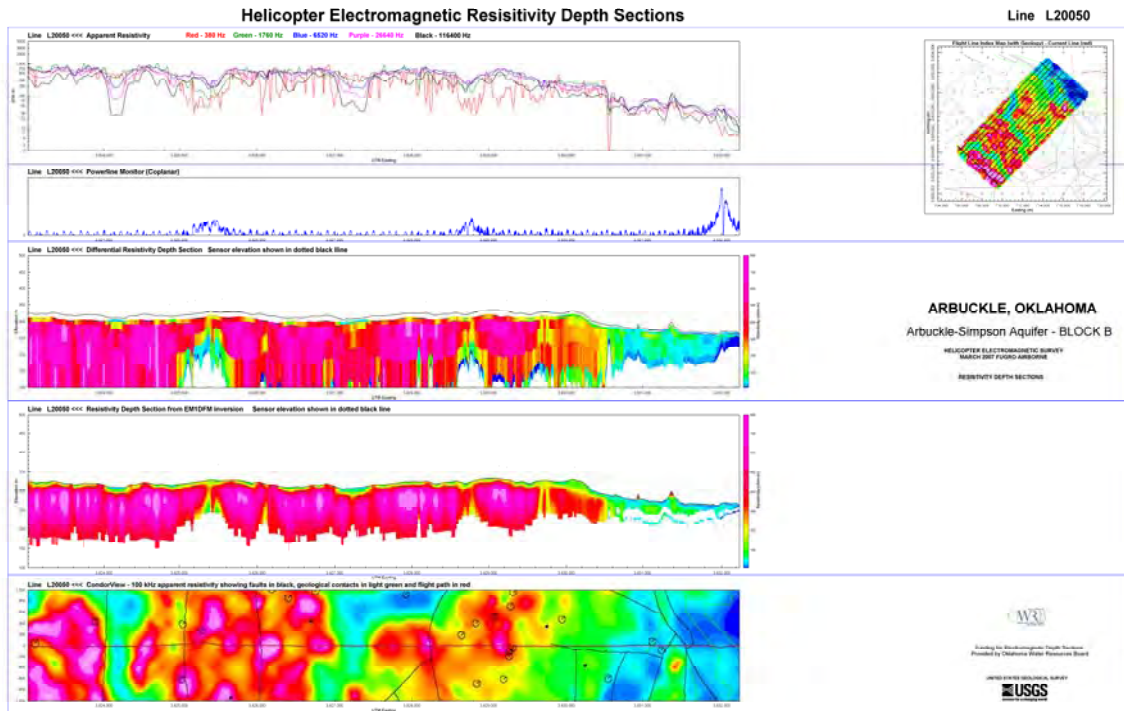


Figure A1-5. Block B Line L20050

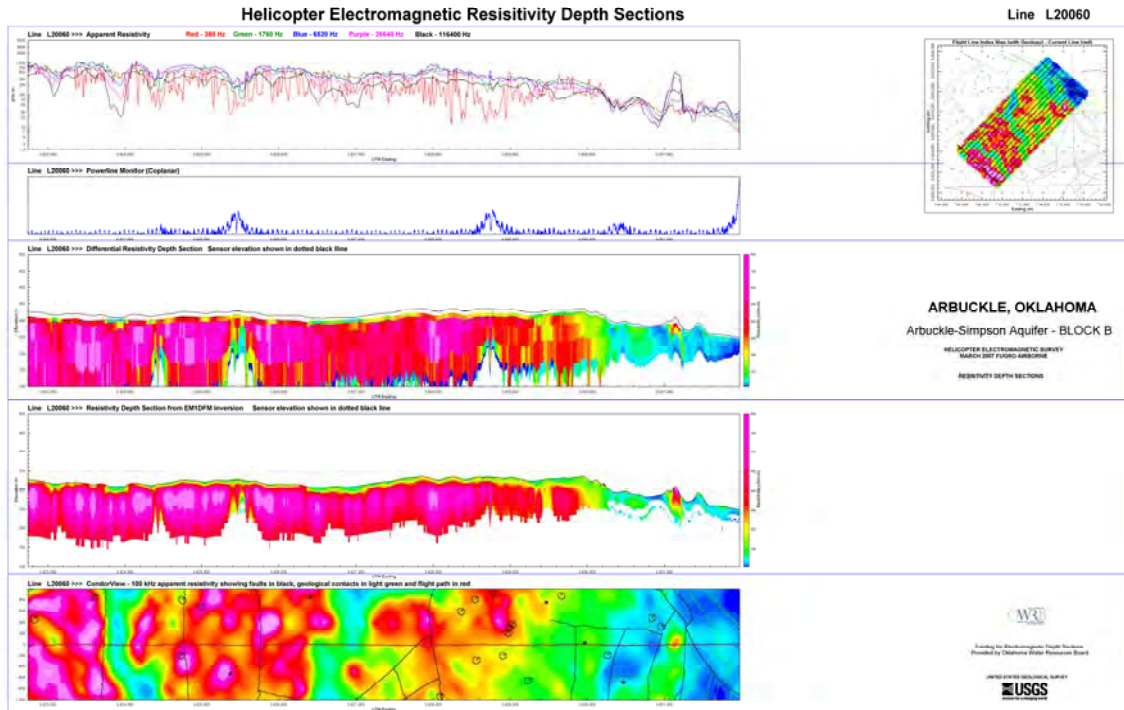


Figure A1-6. Block B Line L20060

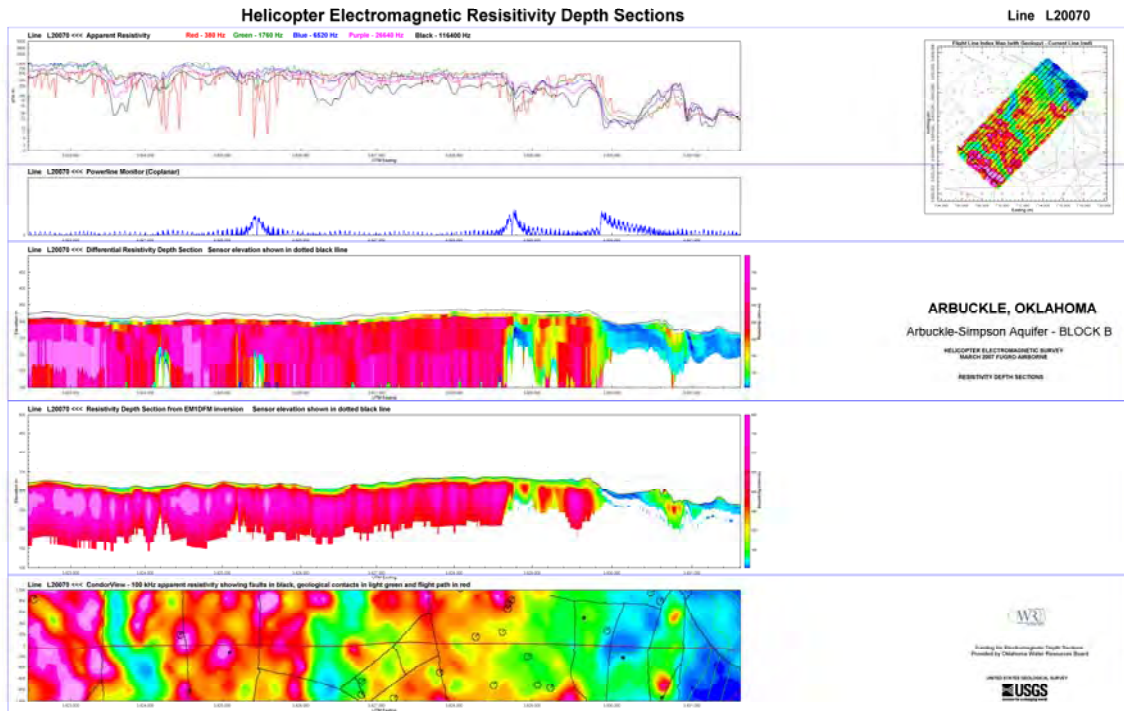


Figure A1-7. Block B Line L20070

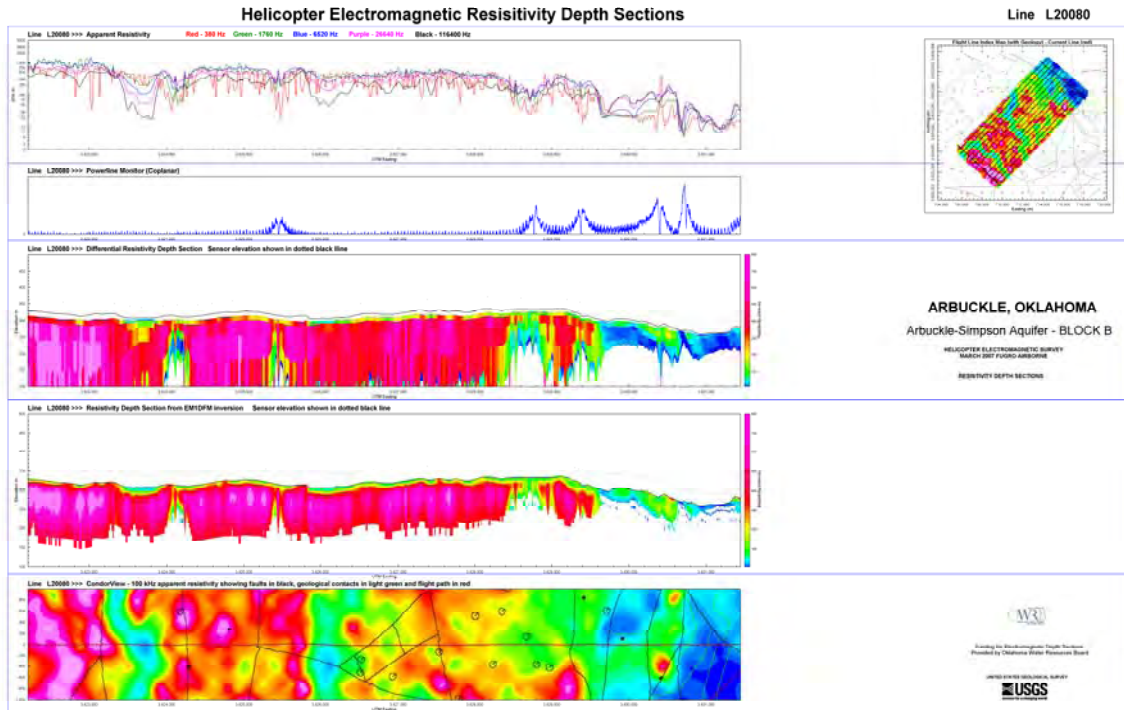


Figure A1-8. Block B Line L20080

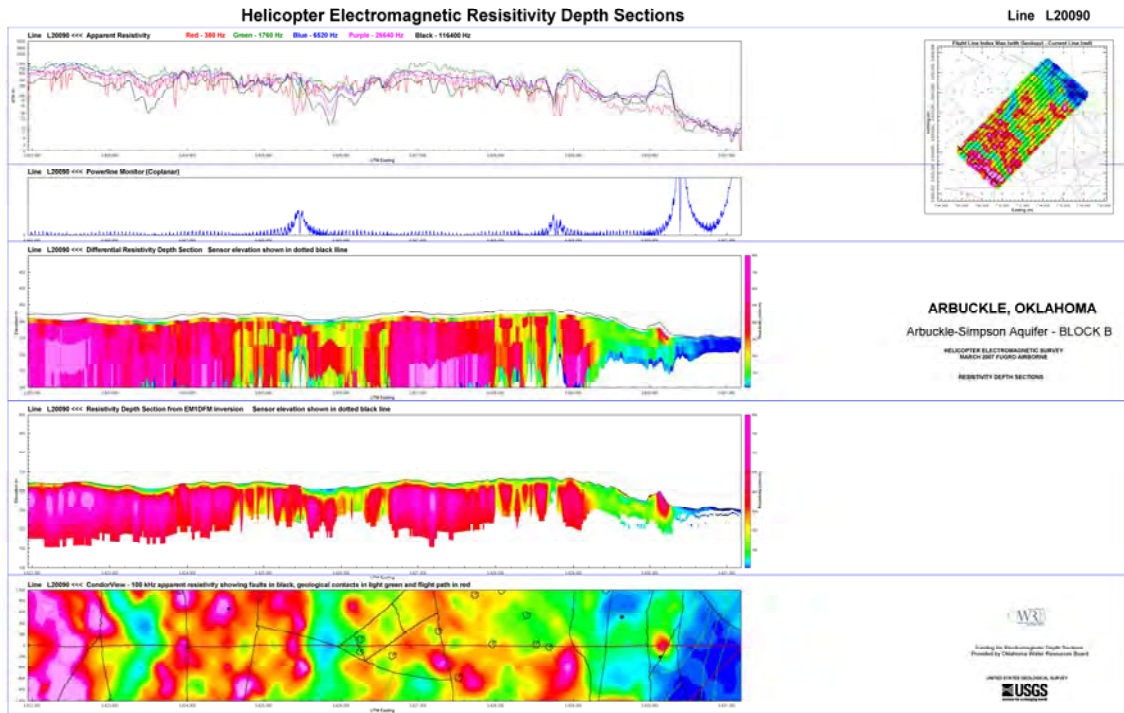


Figure A1-9. Block B Line L20090

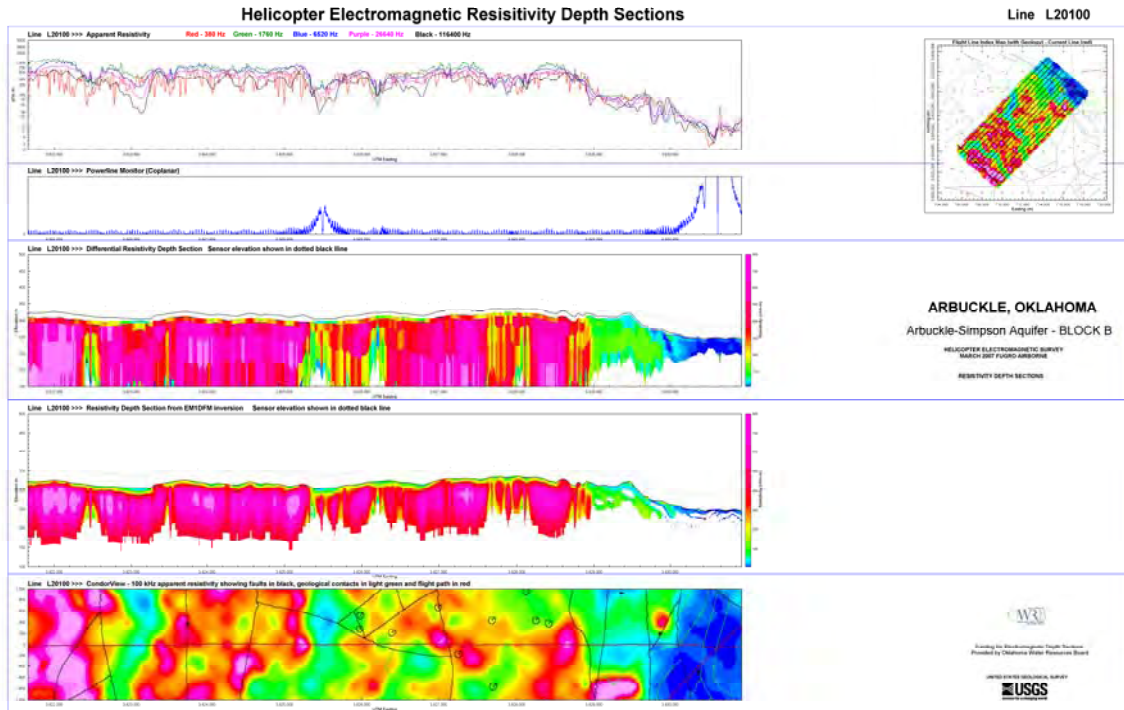


Figure A1-10. Block B Line L20100

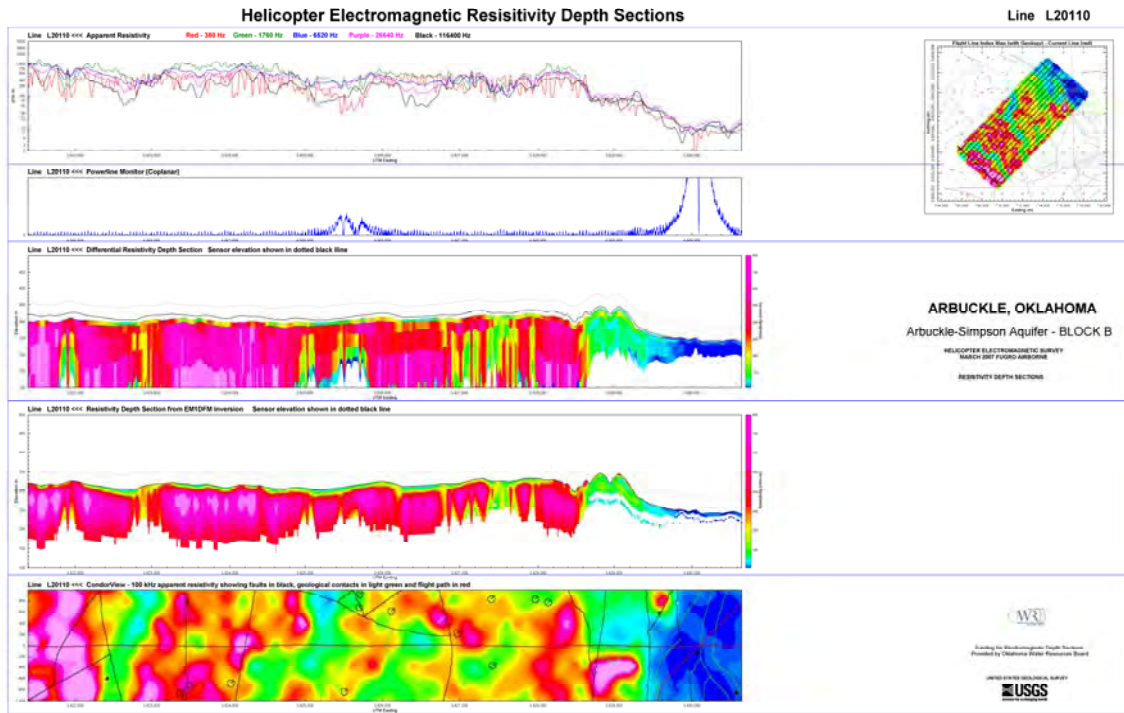


Figure A1-11. Block B Line L20110

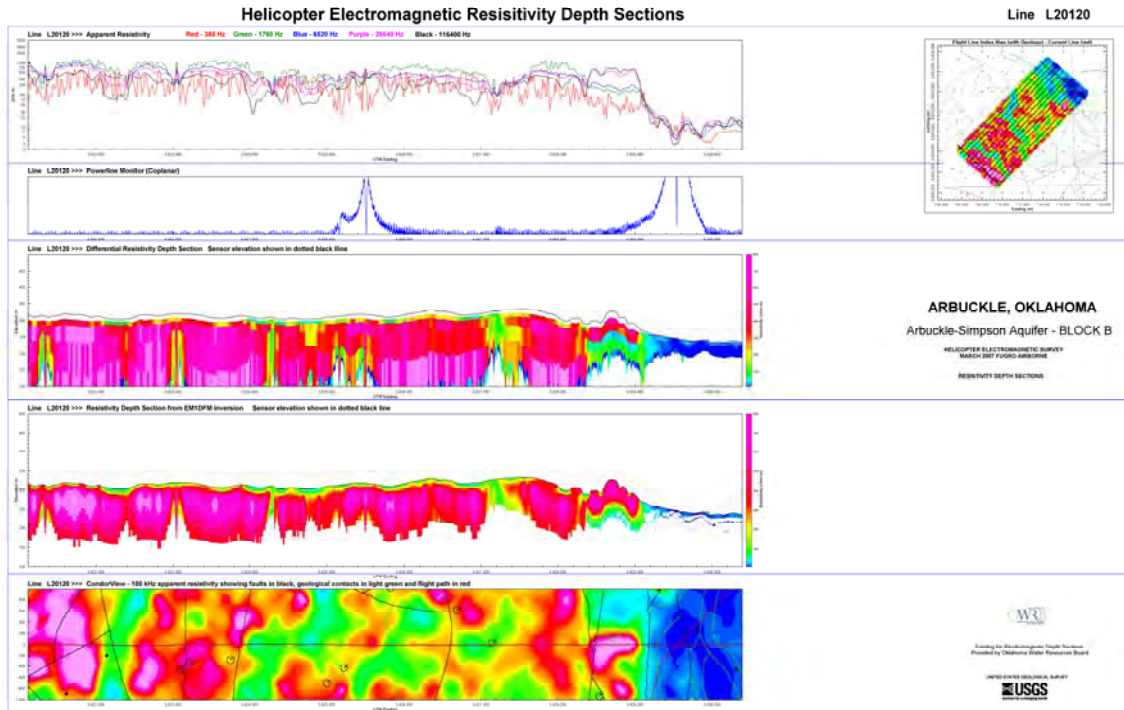


Figure A1-12. Block B Line L20120

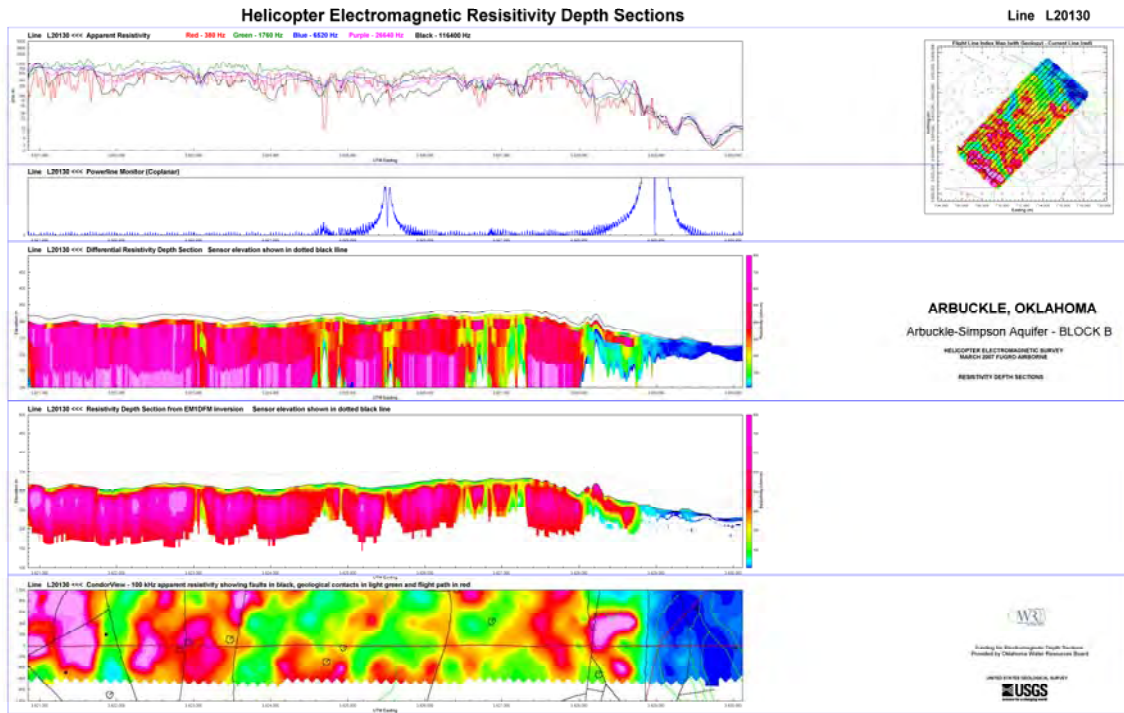


Figure A1-13. Block B Line L20130

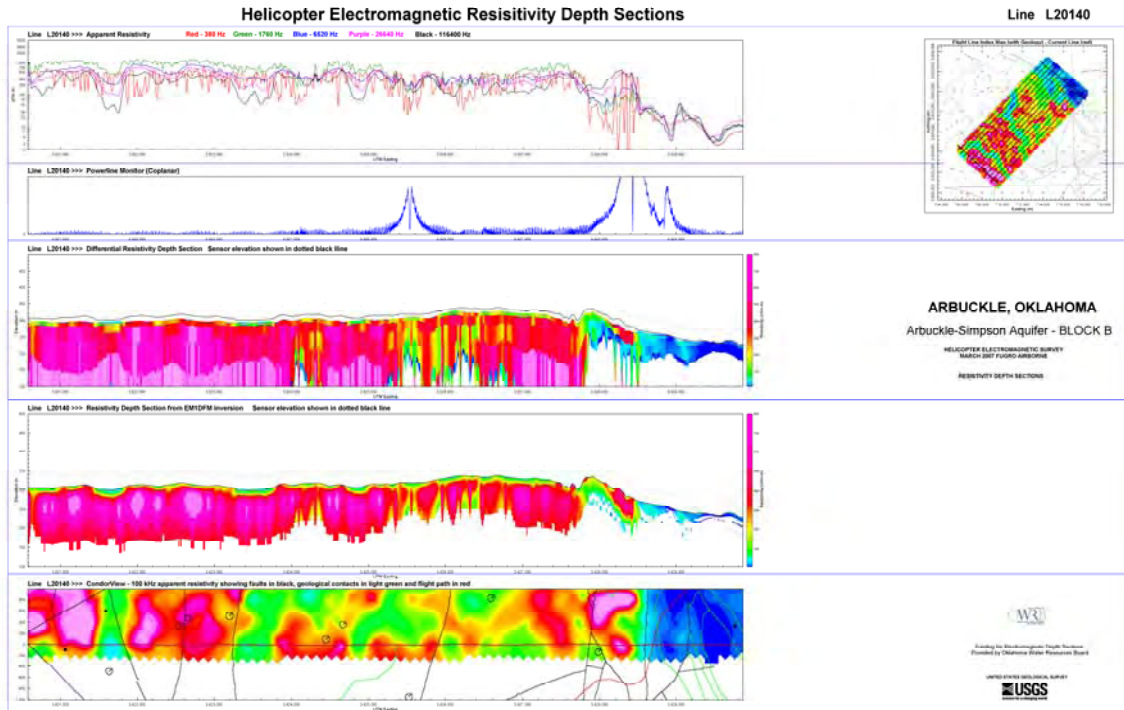


Figure A1-14. Block B Line L20140

Appendix 2. Block D MultiPlots

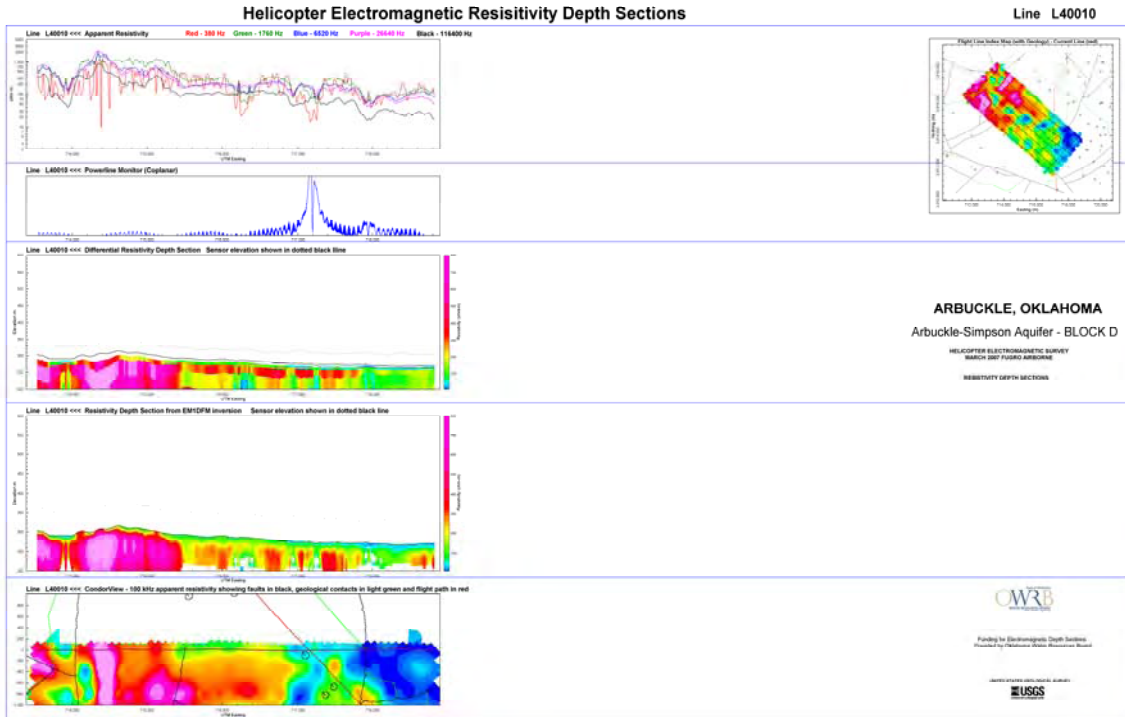


Figure A2-1. Block D Line L40010

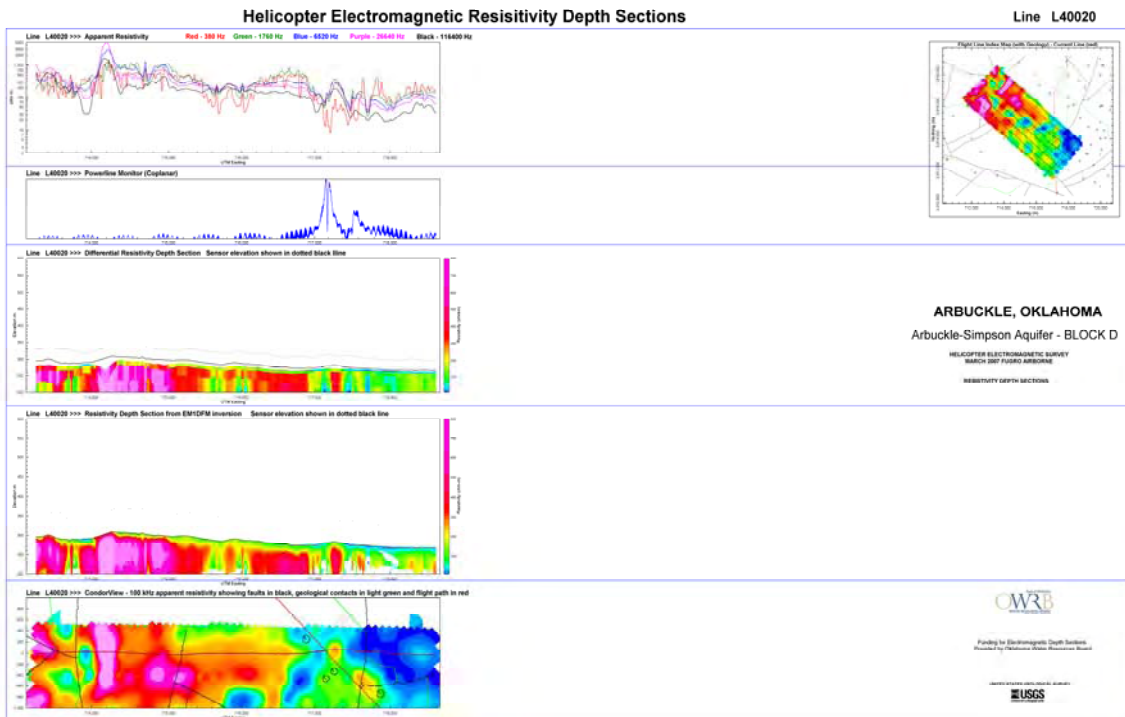


Figure A2-2. Block D Line L40020

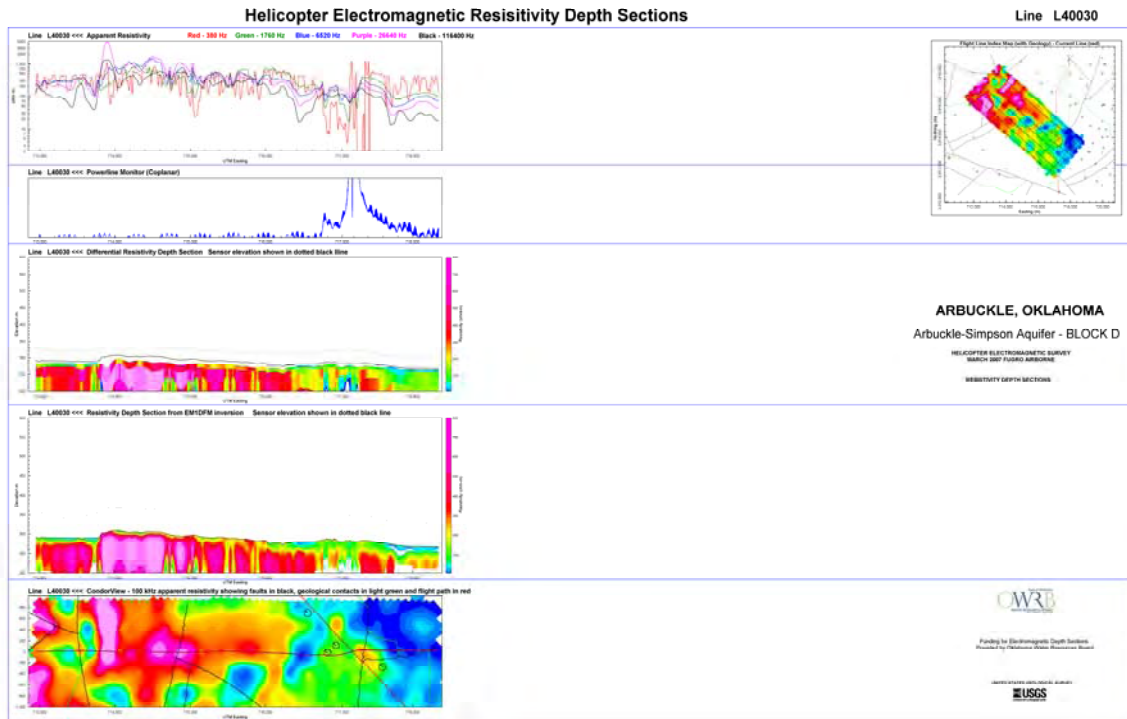


Figure A2-3. Block D Line L40030

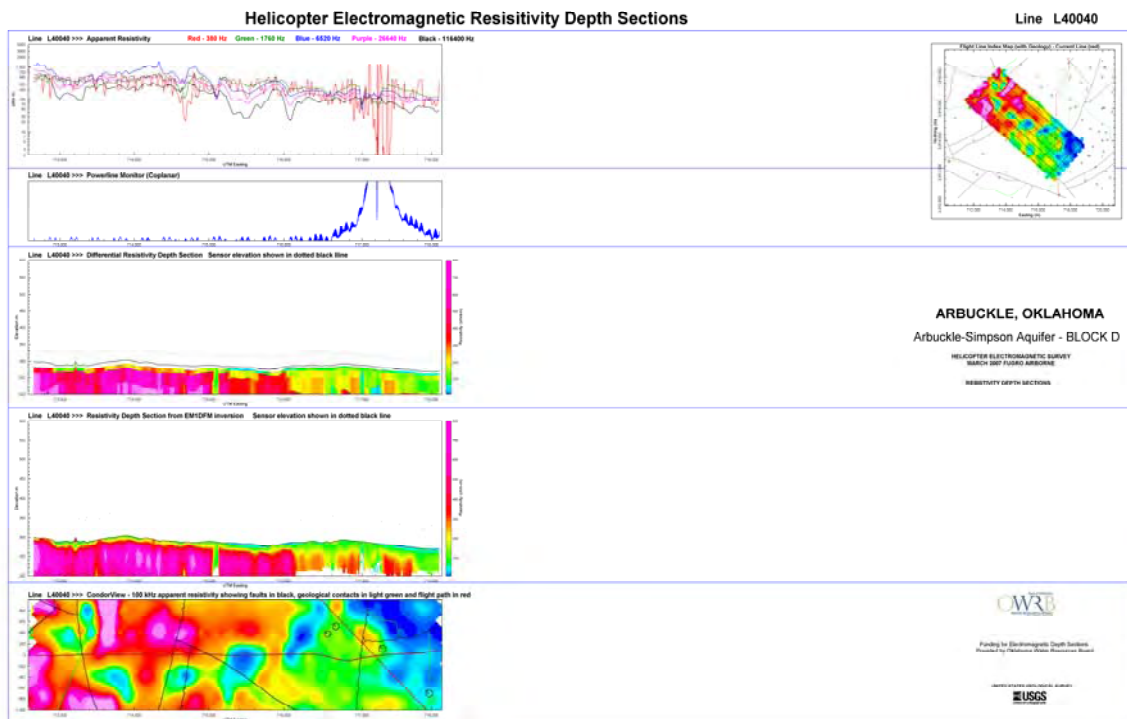


Figure A2-4. Block D Line L40040

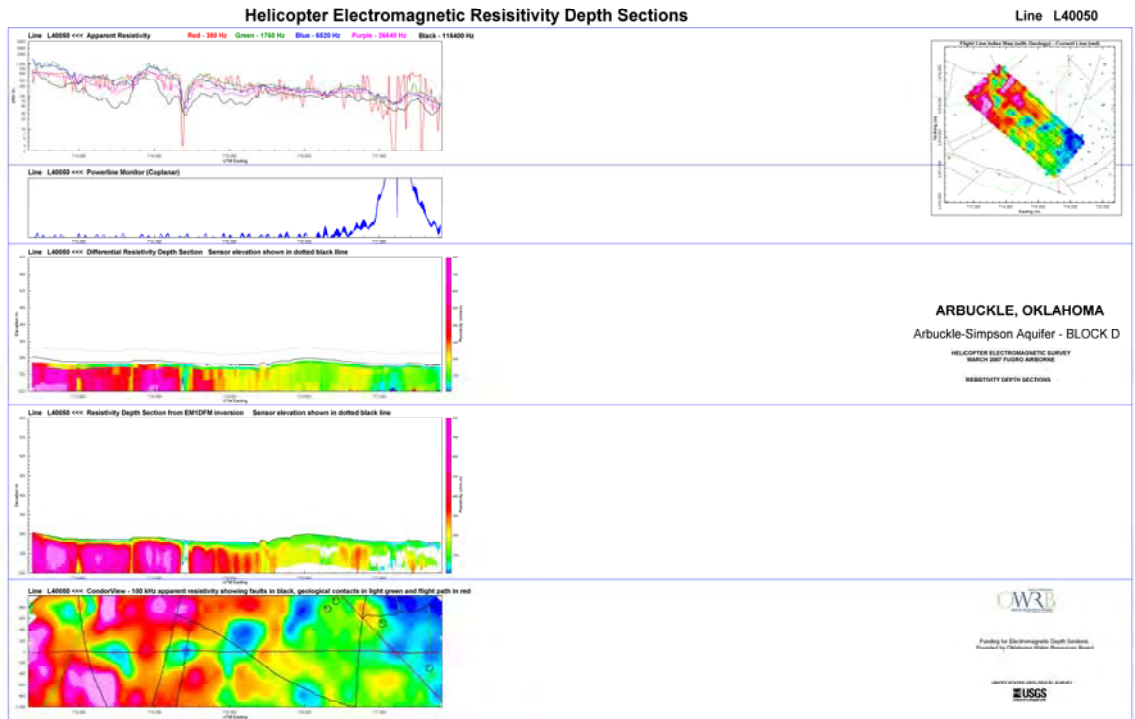


Figure A2-5. Block D Line L40050

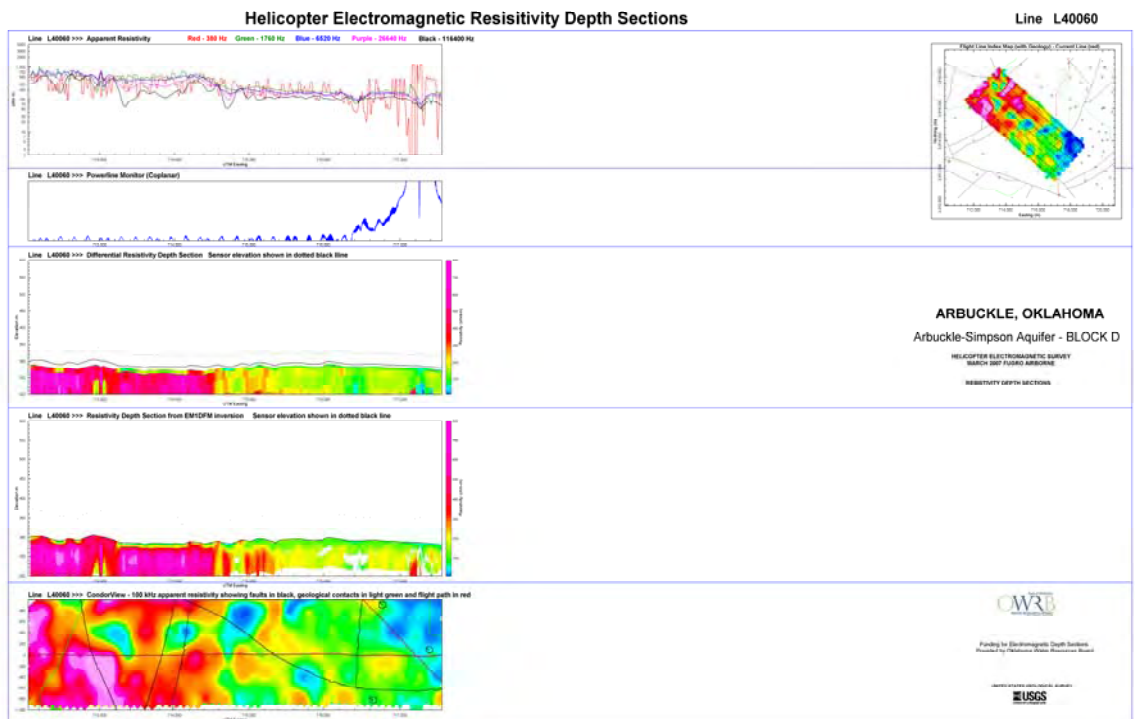


Figure A2-6. Block D Line L40060

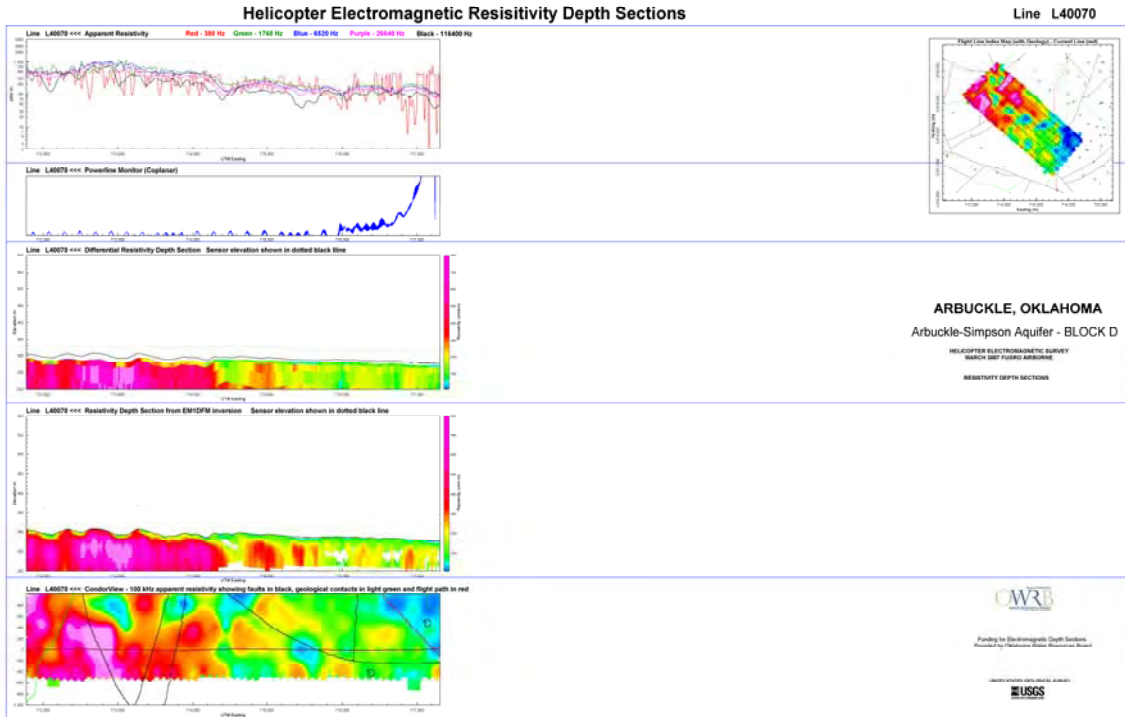


Figure A2-7. Block D Line L40070

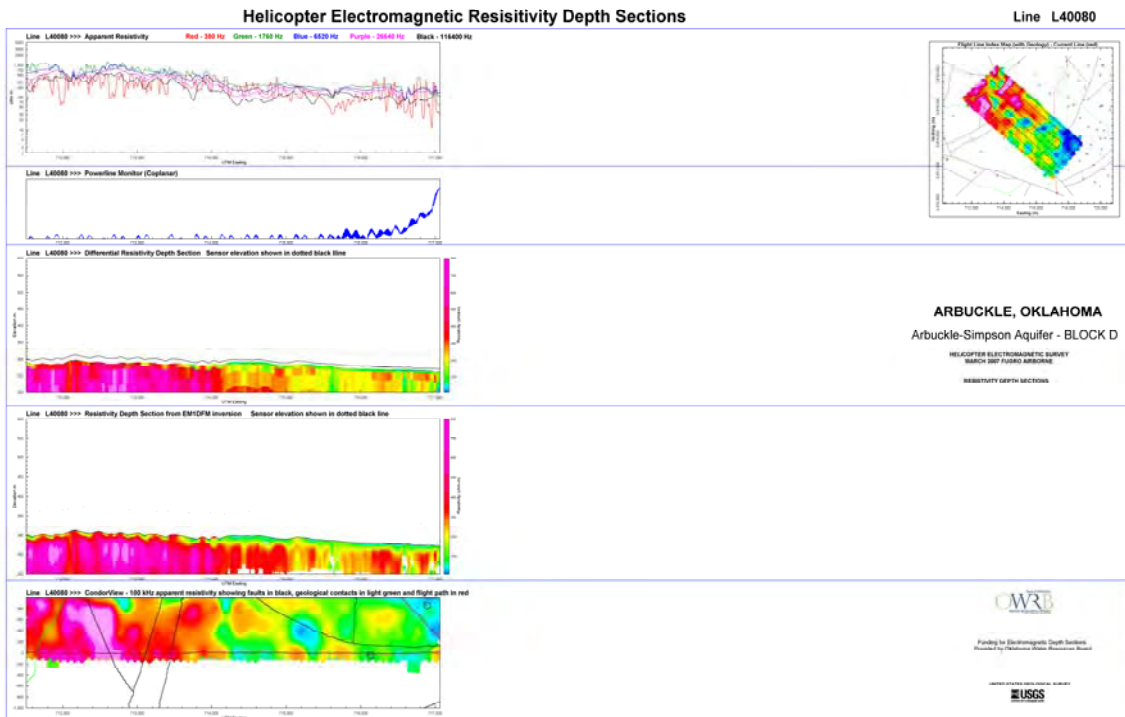


Figure A2-8. Block D Line L40080